

2. EXPLANATORY NOTES¹

Shipboard Scientific Party²

INTRODUCTION

Leg 196 revisited sites previously cored during Ocean Drilling Program (ODP) Legs 131 and 190, and focused on in situ measurements of subseafloor physical properties, pressure, and temperature using two techniques: logging while drilling (LWD) and Advanced CORK (ACORK) long-term hydrogeologic observatories. This chapter explains the operations of the LWD tools and the analysis methods used to arrive at the interpretations reported in the site chapters in this volume. This chapter also describes in some detail the design features and components that are common to the ACORKs deployed in Holes 1173B and 808I. One important feature of the ACORK design is that coring is possible through an ACORK after it is installed; a feature that allowed us to core into basement at Hole 1173B. Hence, we also present the methods used to visually describe and perform physical properties, petrological, geochemical, and paleomagnetic analyses.

LOGGING WHILE DRILLING

Introduction

During Leg 196, four Anadrill LWD and measurement-while-drilling (MWD) tools were deployed. These tools were provided by Schlumberger-Anadrill services under contract with the Lamont-Doherty Earth Observatory Borehole Research Group. LWD surveys have been successfully conducted during six previous ODP legs: Leg 156 (Shipley, Ogawa, Blum, et al., 1995), Leg 170 (Kimura, Silver, Blum, et al., 1997), Leg 171A (Moore, Klaus, et al., 1998), Leg 174A (Austin, Christie-Blick, Malone, et al., 1998), Leg 188 (O'Brien, Cooper, Richter, et al., 2001), and Leg 193 (Binns, Barriga, Miller, et al., 2002). During Leg 196, LWD oper-

¹Examples of how to reference the whole or part of this volume.

²Shipboard Scientific Party addresses.

ations were planned for three sites near the toe of the Nankai accretionary prism. Wireline logs have been difficult to obtain during previous ODP legs in the region (Legs 131 and 190) due to unstable hole conditions. Because coring cannot be conducted while using LWD tools, the coring results from previous legs were correlated with the LWD/MWD data collected during Leg 196.

LWD and MWD tools measure different parameters. LWD tools measure in situ formation properties with instruments that are located in the drill collars immediately above the drill bit. The LWD and MWD tools used during Leg 196 include the resistivity-at-the-bit (RAB) tool, the power pulse MWD tool, the Anadrill Integrated Drilling Evaluation and Logging (IDEAL) sonic-while-drilling (ISONIC) velocity tool, and the azimuthal density neutron (ADN) tool. This was the first time the ISONIC tool was used during an ODP leg. Figure F1 shows the configuration of the LWD/MWD bottom hole assembly (BHA). Table T1 lists the set of measurements recorded.

LWD measurements are made shortly after the hole is cut, and before the adverse effects of continued drilling or coring operations. Fluid invasion into the borehole wall is also reduced relative to wireline logging because of the shorter elapsed time between drilling and taking measurements. MWD tools measure downhole drilling parameters (e.g., weight on bit, torque, etc.). The key difference between LWD and MWD tools is that LWD data are recorded into downhole memory and retrieved when the tools reach the surface, whereas MWD data are transmitted through the drilling fluid within the drill pipe by means of a modulated pressure wave (mud pulsing) at ~3 bits/s and monitored in real time. The term LWD is often used more generically to cover both LWD and MWD type measurements.

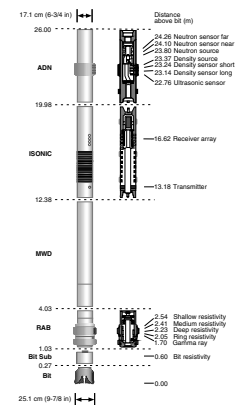
The LWD equipment is battery powered and uses erasable/programmable read-only memory chips to store the logging data until they are downloaded. The LWD tools take measurements at evenly spaced time intervals and are synchronized with a system on the rig that monitors time and drilling depth. After drilling, the LWD tools are retrieved and the data downloaded from each tool through an RS232 serial link to a laptop computer. Synchronization of the uphole and downhole clocks allows merging of the time-depth data (from the surface system) and the downhole time-measurement data (from the tools) into depth-measurement data files. The resulting depth-measurement data are transferred to the processing systems in the Downhole Measurements Laboratory (DHML) for reduction and interpretation.

Depth Tracking Systems

Unlike wireline tools, LWD tools record data in time. The IDEAL surface system records the time and depth of the drill string below the rig floor. LWD operations aboard the *JOIDES Resolution* require accurate and precise depth tracking and the ability to independently measure and evaluate the movement of the following (Fig. F2):

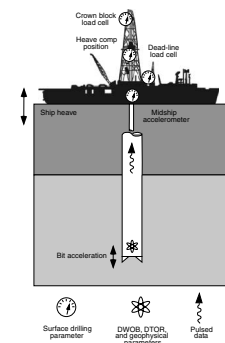
1. Position of the traveling block in the derrick,
2. Heave of the vessel by the action of waves/swells and tides, and
3. Action of the motion compensator.

F1. Configuration of the drill string used for logging operations, p. 30.



T1. LWD tool acronyms and units, p. 48.

F2. Schematic figure of rig instrumentation, p. 31.



Motion Compensator and Drawworks Encoders

The length of the drill string (combined lengths of the BHA and the drill pipe) to the top drive and the position of the top drive in the derrick is used to determine the exact depth of the drill bit and rate of penetration. The system configuration is illustrated in Figure F2.

1. Drilling line is spooled on the drawworks. From the drawworks the drilling line extends to the crown blocks, which are located at the very top of the derrick, and then down to the traveling blocks. The drilling line is passed several times, usually six or eight times, between the traveling blocks and the crown blocks and then fastened to a fixed point called the dead-man anchor. From the driller's console the driller controls the operation of the drawworks, which, via the pulley system described above, controls the position of the traveling blocks in the derrick.
2. On the *JOIDES Resolution*, the heave motion compensator is suspended from the traveling blocks. The top drive is then attached to the motion compensator. The motion compensator uses pistons that are held to a precharge and are, thus, able to provide a buffer against the waves and swell. As the vessel rises, the compensator extends the pistons under the pressure of the precharge to keep the bit on bottom, whereas when the vessel drops, the pistons retract and diffuse any extra weight from being stacked on the bit.
3. The drill string is connected to the top drive; therefore, movement of the top drive needs to be measured to provide the drill string depth.

To measure the movement of the traveling blocks a drawworks encoder (DWE) is mounted on the shaft of the drawworks. One revolution of the drawworks will pay out a certain amount of drilling line and in turn move the traveling blocks a certain distance. Calibration of the movement of the traveling block to the revolutions of the drawworks is required.

Hookload Sensor

A hookload sensor is used to measure the weight of the load on the drill string and can be used to detect whether the drill string is in-slips or out-of-slips. When the drill string is in-slips, motion from the blocks or motion compensator will not have any effect on the depth of the bit (i.e., it will remain stationary), and the DWE information does not augment the recorded bit depth. When the drill string is out-of-slips (drilling ahead), the DWE information augments the recorded bit depth. The difference in hookload weight between in-slips and out-of-slips is very distinguishable. The heave of the ship will still continue to affect the bit depth whether the drill string is in-slips or out-of-slips.

Heave Motion Sensors

On the *JOIDES Resolution* the ability to measure the vessel's heave is addressed in two ways. The rig instrumentation system used by the driller measures and records the heave of the ship and the motion of the cylinder of the active compensator, among many other parameters, at the rig floor. The motion compensator cylinder either extends or re-

tracts to compensate for ship heave that is detected by fixed accelerometers. Both the heave value and cylinder position measurement are transmitted to the Anadrill recording system via the Wellsite Information Transfer System (WITS) line.

Software filtering may be used to smooth the time-depth file by applying a weighted average to the time-depth data based on the observed amplitude and period of ship heave. The depth filtering technique has significantly improved the quality of RAB image logs from previous ODP holes.

RAB Tool

The RAB tool provides resistivity measurements and electrical images of the borehole wall, similar to the Formation MicroScanner but with complete coverage of the borehole walls and lower vertical and horizontal resolution. In addition, the RAB tool contains a scintillation counter that provides a total gamma ray measurement (Fig. F3). Because a caliper log is not available without other LWD measurements, the influence of the shape of the borehole on the log responses cannot be directly estimated.

The RAB tool is connected directly above the drill bit and uses the lower portion of the tool and the bit as a measuring electrode. This allows the tool to provide a bit resistivity measurement with a vertical resolution just a few inches longer than the length of the bit. A 1½-in (4 cm) electrode is located 3 ft (91 cm) from the bottom of the tool and provides a focused lateral resistivity measurement (R_{RING}) with a vertical resolution of 2 in (5 cm). The characteristics of R_{RING} are independent of where the RAB tool is placed in the BHA and its depth of investigation is ~7 in (18 cm). In addition, button electrodes provide shallow-, medium-, and deep-focused resistivity measurements as well as azimuthally oriented images. These images can then reveal information about formation structure and lithologic contacts. The buttons are ~1 in (2.5 cm) in diameter and reside on a clamp-on sleeve. The buttons are longitudinally spaced along the RAB tool to render staggered depths of investigation of ~1, 3, and 5 in (2.5, 7.6, and 12.7 cm). The tool's orientation system uses the Earth's magnetic field as a reference to determine the tool position with respect to the borehole as the drill string rotates, thus allowing both azimuthal resistivity and gamma ray measurements. Furthermore, these measurements are acquired with an ~6° resolution as the RAB tool rotates. Vertical resolution and depth of investigation for each resistivity measurement are shown in Table T2.

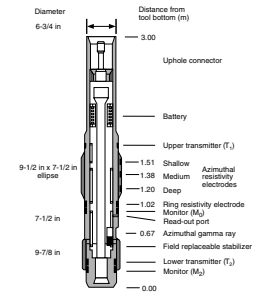
The RAB tool collar configuration is intended to run in 8½-in (22 cm) and 9⅞-in (25 cm) diameter holes depending on the size of the measuring button sleeve. During Leg 196, we used a 9⅞-in-diameter bit and a 9⅞-in-diameter button sleeve for the RAB tool. This resulted in a “zero-gap” standoff between the resistivity buttons and the formation, giving higher resolution images.

RAB Tool Specifications

Bit Resistivity Measurements

For the bit resistivity measurements, a lower transmitter (T_2) produces a current and a monitoring electrode (M_0) located directly below the ring electrode measures the current returning to the collar (Fig. F3). When connected directly to the bit, the RAB tool uses the lower few

F3. RAB tool, p. 32.



T2. RAB measurement resolution and depth of investigation, p. 49.

inches of the RAB tool as well as the bit as a measurement electrode. The resultant resistivity measurement is termed R_{BIT} and its depth of investigation is ~12 in (30.48 cm).

Ring Resistivity Measurements

The upper and lower transmitters (T_1 and T_2) produce currents in the collar that meet at the ring electrode. The sum of these currents is then focused radially into the formation. These current patterns can become distorted depending on the strength of the fields produced by the transmitters and the formation around the collar. Therefore, the RAB tool uses a cylindrical focusing technique that takes measurements in the central (M_0) and lower (M_2) monitor coils to reduce distortion and create an improved ring response. The ring electrode is held at the same potential as the collar to prevent interference with the current pattern. The current required for maintaining the ring at the required potential is then measured and related to the resistivity of the formation. Because the ring electrode is narrow (~4 cm), the result is a measurement (R_{RING}) with 5-cm vertical resolution.

Button Resistivity Measurements

The button electrodes function the same way as the ring electrode. Each button is electrically isolated from the body of the collar but is maintained at the same potential to avoid interference with the current field. The amount of current required to maintain the button at the same potential is related to the resistivity of the mud and formation. The buttons are 4 cm in diameter and the measurements (R_{BUTTON}) can be acquired azimuthally as the tool rotates within 56 sectors to produce a borehole image.

RAB Programming

For quality control reasons, the minimum data density is one sample per 6-in (15.2 cm) interval; hence, a balance must be determined between the rate of penetration (ROP) and the sampling rate. This relationship depends on the recording rate, the number of data channels to record, and the memory capacity (5 MB) of the LWD tool. The relationship between ROP and sample rate is as follows:

$$\text{ROP(ft/hr)} = 1800/\text{sample rate(s)} \text{ and}$$

$$\text{ROP(m/hr)} \approx 548/\text{sample rate(s)}.$$

This equation defines the fastest ROP allowed at a given sample rate to produce one sample per 6-in interval. Using a sample rate of 10 s for high-quality image resolution, the maximum ROP is ~55 m/hr. For Leg 196, the target ROP was 35–50 m/hr, improving the vertical resolution to 3 in. Under this configuration the RAB tool has enough memory to record 42 hr of data. That is enough time to complete LWD operations over an ~1000-m interval at 25 m/hr ROP, or an 1200-m interval at 30 m/hr ROP. To achieve the deeper Leg 196 targets or their shallow companion holes, the sampling rate had to be lower and/or the ROP had to be higher.

downward direction along the borehole. Drilling noise is always present, and in order to minimize its effect we attempted to keep pump rate, ROP, and drill pipe rotation as low as possible.

Since the upward propagation of energy in the formation is synchronized with the transmitter firing and any residual drilling noise is not, averaging the waveforms from various consecutive firings will decrease the relative importance of incoherent signals. A stack size of approximately eight waveforms is deemed appropriate for these conditions. The ISONIC tool must also be kept centralized in the borehole in order to maximize the strength of the formation signal for stacked waveforms. In large holes and slow sediments, both the formation itself and asymmetry of the annular space in the hole will attenuate the signal.

ISONIC Programming and Data Processing

The ISONIC tool is configured so that waveform data are stored at 8-s intervals, allowing for 83 hr of drilling before the downhole memory is filled. This was sufficient to reach the target depth at each of the Leg 196 sites at a ROP of 25 m/hr. The maximum ROP allowable to achieve one sample per 6-in interval is estimated by

$$ROP_{\max} = 1800/8 = 225 \text{ ft/hr} \approx 68 \text{ m/hr.}$$

ISONIC waveform data were converted to depth and processed to estimate *P*-wave slowness and waveform coherence using the Anadrill IDEAL system on the *JOIDES Resolution*. These data, however, are heavily filtered and do not result in optimal measured values in slow formations. The raw ISONIC waveforms (i.e., neither filtered nor compressed) were available in the memory dump file but could not be processed with the IDEAL field software. The data were transmitted to Anadrill (Houston, Texas) for processing, which included bandpass filtering, restacking, waveform slowness-time-coherency analysis, and depth-time merging, to compute the *P*-wave velocity as a function of depth. After processing, the data were returned via satellite transmission to the ship. The velocity curves shown in this report were produced through two iterations of this process; further waveform processing and arrival modeling will be necessary to evaluate log quality.

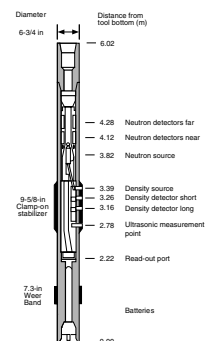
ADN Tool

The ADN tool is similar in principle to the compensated density neutron (CDN) tool (Anadrill-Schlumberger, 1993; Moore, Klaus, et al., 1998). The density section of the tool uses a 1.7-Ci ¹³⁷Cs gamma ray source in conjunction with two gain-stabilized scintillation detectors to provide a borehole-compensated density measurement. The detectors are located 5 and 12 in (12.7 and 30.48 cm) below the source (Fig. F6). The number of Compton scattering collisions (change in gamma ray energy by interaction with the formation electrons) is related to the formation density.

Returns of low energy gamma rays are converted to a photoelectric effect value, measured in barns per electron. The photoelectric effect value depends on electron density and hence responds to bulk density and lithology (Anadrill-Schlumberger, 1993). It is particularly sensitive to low-density, high-porosity zones.

The density source and detectors are positioned behind holes in the fin of a full gauge 9 7/8-in (25.08 cm) clamp-on stabilizer. This geometry

F6. ADN tool, p. 35.



forces the sensors against the borehole wall, thereby reducing the effects of borehole irregularities and drilling. Neutron logs are processed to eliminate the effects of borehole diameter, tool size, temperature, drilling mud hydrogen index (dependent on mud weight, pressure, and temperature), mud and formation salinities, lithology, and other environmental factors (Schlumberger, 1994). The vertical resolution of the density and photoelectric effect measurements is about 15 and 5 cm, respectively.

For measurement of tool standoff and estimated borehole size, a 670-kHz ultrasonic caliper is available on the ADN tool. The ultrasonic sensor is aligned with and located just below the density detectors. In this position the sensor can also be used as a quality control for the density measurements.

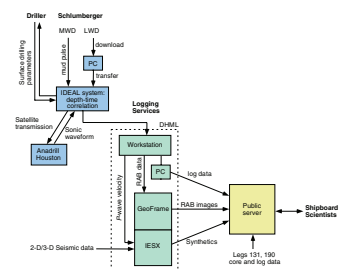
Neutron porosity measurements are obtained using fast neutrons emitted from a 10-Ci americium oxide-beryllium (AmBe) source. Hydrogen quantities in the formation largely control the rate at which the neutrons slow down to epithermal and thermal energies. The energy of the detected neutrons has an epithermal component because much of the incoming thermal neutron flux is absorbed as it passes through the 1-in drill collar. Neutrons are detected in near- and far-spacing detector banks, located 12 and 24 in (30.48 and 60.96 cm), respectively, above the source. The vertical resolution of the tool under optimum conditions is ~34 cm. The neutron logs are affected to some extent by the lithology of the matrix rock because the neutron porosity unit is calibrated for a 100% limestone environment.

The ADN tool does not collect four quadrants of azimuthal data unless the well deviates >~10° from vertical. Data output from the ADN tool includes apparent neutron porosity (i.e., the tool does not distinguish between pore water and lattice-bound water), formation bulk density, and photoelectric effect. The density logs graphically presented here have been “rotationally processed” to show the average density that the tool reads while it is rotating. In addition, the ADN tool outputs a differential caliper record based on the standard deviation of density measurements made at high sampling rates around the circumference of the borehole. The measured standard deviation is compared with that of an in gauge borehole, and the difference is converted to the amount of borehole enlargement (Anadrill-Schlumberger, 1993). A standoff of <1 in between the tool and the borehole wall indicates good borehole conditions, for which the density log values are considered to be accurate to ±0.015 g/cm³ (Anadrill-Schlumberger, 1993).

Onboard Data Flow

Figure F7 shows onboard data flow during Leg 196. Surface drilling parameters and MWD data were directly transmitted to the Schlumberger IDEAL system. A laptop PC was used to download and transfer the LWD data from the tools on the rig floor to the IDEAL system for depth-time correlation. The log data were then distributed to the shipboard party via the workstation in the DHML. RAB image data were processed and converted to graphic format using GeoFrame on the DHML workstation prior to distribution to the shipboard party. Sonic waveform data were sent to Anadrill in Houston, Texas, via satellite to be reprocessed and then returned to the ship.

F7. Onboard data flow, p. 36.



IDENTIFICATION OF LOG UNITS THROUGH VISUAL INTERPRETATION AND MULTIVARIATE STATISTICAL ANALYSIS

Log units obtained from LWD data at Leg 196 sites were defined through a combination of visual interpretation and multivariate statistical analysis. Log units were identified visually by examining the character of the gamma ray, density, neutron porosity, resistivity, and photoelectric effect curves. First-order log units are related primarily to lithology corresponding to changes in the log character. Second-order log units represent subtle changes in log data, which are possibly non-lithologic.

Multivariate statistical analysis provided objective confirmation of the log unit boundaries. The multivariate statistical analysis entailed the following steps:

1. Each logging curve was normalized by subtracting the mean and then dividing by the standard deviation. The resulting curves have a mean of zero and a standard deviation of 1.
2. Factors and factor loadings were calculated from the normalized curves using standard R-mode factor analysis procedures, with Kaiser Varimax factor rotation as described, for example, by Davis (1973). Each factor is simply a linear combination of the input variables weighted by the factor loadings; the factors can be visualized as a projection of n input variables (the normalized logging data) onto n linearly independent (uncorrelated) principal axes. Generally, for the Leg 196 LWD data sets, more than 75% of the variance observed in the input variables can be described by the first three factors.
3. The factors were then decimated to a 1-m depth interval using a finite-impulse-response, low-pass antialiasing filter to reduce the number of data points. This step was necessary because of computational limits of the software and hardware used for the next step.
4. Finally, a complete linkage hierarchical cluster analysis (using Euclidean norm; Davis, 1973) was performed on the three decimated factors that accounted for the greatest percentage of variance observed in the data. This allowed the identification of electrofacies, or log units, with distinct combinations of logging properties (e.g., Serra, 1986).

Factor analysis is a method of reducing the number of logs without losing important information. Cluster analysis of the three most important factors proved to be a useful and objective method of identifying significant first- and second-order log units.

INTERPRETING STRUCTURE FROM RAB IMAGES

Structural data were determined from RAB images using Schlumberger's Geoframe software. Geoframe presents RAB data as a planar, "unwrapped" 360° resistivity image of the borehole with depth. Horizontal features are horizontal within these images, whereas planar dipping features are sinusoidal. Sinusoids are interactively fitted to beds

and fractures to determine their dip and azimuth, and exported from Geoframe for further analysis.

Methods of interpreting structure and bedding differ considerably between Leg 131, Site 808 and Leg 190, Site 1173 (core analysis and wireline Formation MicroScanner [FMS] images) and Leg 196, Sites 808 and 1173 (RAB image analysis). Resolution is considerably lower for RAB image interpretation (5–10 cm at best, compared with millimeters within cores and 0.5 cm for FMS images), and therefore identified features are likely to be different in scale. For example, microfaults (“small faults,” <1 mm width) and shear bands (1–2 mm, up to 1 cm width) identified at Leg 131, Site 808 are not visible in Leg 196 data. This should be considered when directly comparing reports.

Fractures were identified within RAB images by their anomalous resistivity or conductivity and from contrasting dip relative to surrounding bedding trends. Differentiating between fractures and bedding planes is problematic in places, particularly in Hole 808I, as both may be steeply dipping and with similar orientations, based on comparison with the results of Leg 131, Site 808 (Shipboard Scientific Party, 1991b) and seismic data. The interpretations presented here are based on the above criteria but it is acknowledged that fractures and bedding planes may have been misinterpreted in some cases.

CORE-LOG SEISMIC CORRELATION AND SEISMIC RESOLUTION

The results of Legs 131 and 190 and a three-dimensional (3-D) seismic survey were correlated with the Leg 196 LWD data. The correlation included physical properties measurements, wireline logs, velocity data, and two-dimensional and 3-D seismic survey images collected during 11 yr of research at Nankai Trough. To ensure accurate correlation of the data, it was important to ascertain the accuracy of the navigation of each of the associated surveys, the hole deviation, and the drill string position at the seafloor relative to the sea surface, the accuracy of the depth-converted seismic data, and the vertical and horizontal seismic resolution. Accurate correlation is critical to extend the study of the subsurface physical properties away from the direct measurements at the borehole using the 3-D seismic data.

Navigation

During Legs 190 and 196 surface navigation consisted of dynamic positioning at the surface relative to an acoustic beacon at the seafloor at each drill site. Both legs took place after the Global Positioning System (GPS) signal selective availability was removed, thereby providing the accuracy available from P-code GPS. There is no navigation information for the bottom of the drill string, and therefore its exact position relative to the ship’s position is unknown. We assume the hole position to be directly below the rig floor. During previous drilling, deviation of the hole from the ship’s position was determined from cores recovered at shallow depths by the advanced piston corer. Little significant deviation from the vertical was noted.

The 3-D seismic reflection data (Bangs et al., 1999; Moore et al., 2001) was imaged during an 8 km × 80 km volume recorded to 12 s in time-depth. The survey used a differential GPS navigation system pro-

vided by Fugro Geodetic. Three base stations at Okinawa, Seoul, and Sapporo provided differential corrections at 1 Hz. Fixes were smoothed with a 15-s running average filter to eliminate ship's motion and determine shot locations in real time. The single 6-km streamer was navigated with differential GPS fixes transmitted back from the tail buoy and with compass readings at 300-m intervals along the streamer. Streamer configuration was constructed from compass data for each shot. Tests of navigation accuracy conducted in port show that the ships's position fell within a 2-m radius 95% of the time. During the experiment, the streamer was located better or worse by reconstructing the streamer with the compass readings. Locations are better in the direction parallel to the stream than perpendicular to it. In the parallel direction, 90% of the estimated streamer locations lay within ± 10 m of the differential GPS position. Perpendicular to the streamer, 90% of the estimated locations lay within ± 50 m of the tail buoy differential GPS position.

Seismic Resolution

Horizontal and vertical resolution of the 3-D seismic images is dependent on the data frequency content, which becomes more bandwidth limited with depth of penetration. The Nankai Trough 3-D seismic data have an approximate bandwidth of 8–65 Hz and a dominant frequency of 33–40 Hz depending on depth below the seafloor. The vertical resolution of these data is therefore 10–15 m based on resolving distinctions of one-quarter of the dominant frequency's wavelength. The common midpoint spacing of 25 m in the inline and 50 m in the crossline direction effectively integrates the seismic acoustic impedance data over an estimated first Fresnel zone radius of ~ 290 m at the seafloor.

First-order depth conversions of the seismic reflection data were calculated using major seismic horizons correlated to the core and log data from Leg 190. Further refinements to the velocity model used for time-to-depth conversions have been carried out through iterative prestack depth migration (Hills et al., 2001) and through velocities obtained from the wireline and core data.

Seismic Waveform Modeling

In order to correlate the 3-D seismic data with the LWD data, synthetic seismograms were constructed using the best densities and velocities for each site from the LWD density, core density, wireline *P*-wave velocity, core *P*-wave velocity, and ISONIC *P*-wave velocity measurements. The 256-ms long-source wavelet used at each site was calculated deterministically using 10 traces from the seafloor reflection centered at Hole 1173B.

ACORK BOREHOLE HYDROGEOLOGIC OBSERVATORIES

Background

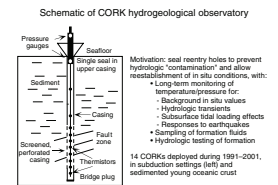
Starting in the late 1980s, ODP engineers and scientists developed instrumentation to hydrologically seal-cased boreholes at the seafloor, simultaneously emplacing long-term instrumentation in the sealed

holes. These hydrogeologic observatories are called CORKs (Davis et al., 1992; Davis and Becker, 1993). CORKs (Fig. F8) allow the formation state to be monitored continuously for years after drilling, with the aim of understanding in situ hydrological processes after recovery from drilling-induced disturbances, which have been documented to persist for years in unsealed reentry holes. In 1991, the first CORKs were installed during Leg 139 in two holes drilled through sediment and into igneous basement in the Middle Valley rift of the northernmost Juan de Fuca Ridge (Davis and Becker, 1994). Other sites followed, including two in the Cascadia accretionary prism (Davis et al., 1995), two in the Barbados accretionary prism (Becker et al., 1997; Foucher et al., 1997), four on the eastern Juan de Fuca Ridge flank (Davis and Becker, 1998, 1999), one on the western Mid-Atlantic Ridge flank (Davis et al., 2000; Becker et al., 2001), and most recently one in a Mariana forearc serpentinite diapir (Salisbury, Shinohara, Richter, et al., 2002). While the specific objectives of these installations have differed, all of the monitoring experiments have made use of the basic CORK capabilities to monitor temperatures at multiple depths and seafloor and formation pressures over long periods of time. Beginning with the Barbados installations, fluid samplers were added to some of the temperature sensor cables to allow continuous sampling of deep-formation water. At several of the CORK sites additional sampling and hydrologic testing experiments have been completed using valves that allow controlled access to the sealed sections (e.g., Sreaton et al., 1995, 1997).

These original CORKs succeeded in preventing borehole flow, allowed average formation pressures to be measured accurately, and allowed temperatures to be determined accurately at multiple depths. However, use of only a single seal meant that the formation pressure observations and fluid samples were integrated over the open sections of the holes, either from the entire open hole sections of igneous basement beneath the casing or through sections of perforated casing within sediments. In other words, determinations of local pressure or compositional gradients were not possible other than for the total interval from the seafloor to the level of the observation. This limitation, as well as the success of the initial CORK design, stimulated great interest in enhancing the capabilities to include monitoring of multiple zones in a single hole, corresponding more closely to natural hydrogeologic structures, with a greater range of sensor capabilities.

These objectives have now been addressed with the ACORK (Becker and Davis, 1998, 2000), designed for a variety of applications and installed for the first time during Leg 196 for a long-term monitoring experiment in the Nankai Trough accretionary prism. The design takes greater advantage of individual boreholes by utilizing packers and screens to allow pressures and compositions to be observed at multiple levels, just as is often done in terrestrial hydrologic experiments. The system consists of a 10.75-in outside-diameter (OD), 10.05-in inside-diameter (ID) casing string with modular packer and screened monitoring elements positioned at desired depths. Pressure monitoring and fluid sampling is done via a multiline hydraulic umbilical strapped to the outside of the casing. The hydraulic lines from each level pass successively through packers and screens above, then are plumbed into a seafloor framework that houses sampling and testing ports, pressure sensors, and data loggers. The numbers of packer and screen elements are limited only by cost, deployment logistical considerations, and the space needed for the total number of hydraulic lines that must pass through the uppermost element. Once the casing with its packers and

F8. Schematic of CORK hydrogeologic observatory, p. 37.



screens is in place and a bridge plug is installed to seal the casing at its deepest point, the inside of the ACORK string becomes hydrologically isolated from the formation. In this way, full-diameter access is provided for downhole instruments to the total depth of the installation without perturbing the pressure monitoring. A small-diameter reentry cone at the top of the ACORK frame allows instrument installations at any time by wireline. It also allows reentry from a drilling vessel for hole deepening or sensor installations below the bridge plug and casing.

ACORK Technical Details

Summary of Installation and Configuration

The sandy turbidites deposited along the Nankai Trough axis are unstable, and casing was required to prevent collapse of this portion of the holes, both for LWD and ACORK operations. Hence, the first step in completing the ACORK installations was to install reentry cones and 20-in casing to 121 mbsf in Hole 1173B and 157 mbsf in Hole 808I (Fig. F9A). LWD operations followed immediately, with penetration to 3 m below the top of basement in Hole 1173B and to ~30 m below the décollement zone in Hole 808I (Fig. F9B). Although basement was targeted at Site 808, hole instability at the décollement zone and the resistance to circulation caused by centralizers above the logging tool assembly limited penetration to just below the décollement zone.

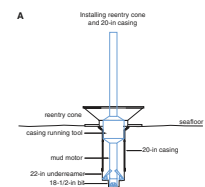
The 9 $\frac{7}{8}$ -in LWD holes completed during the first three weeks of Leg 196 served as “pilot holes” and were enlarged to 17 $\frac{1}{2}$ in for the ACORK assembly (Fig. F9C). Formation conditions were well defined by the experience gained through both the LWD and hole-opening operations, and the combination of LWD data with coring and wireline logging results from Legs 131 and 190 defined the targets for ACORK monitoring intervals and the total depths that could be reached. The scientific rationale for the choice of specific monitoring zones and packer depths for the installations in Holes 808I and 1173B is described in the site chapters in this volume.

After each hole was opened, the ACORK string, including screens, packers, hydraulic lines, seafloor frame, sensors, and data logger (described in detail below), was made up for reentry. The string was hung off on a BHA that included an ACORK running tool, pipe, drill collars, a mud motor, and a pilot bit plus underreamer with collapsible arms, positioned just below the deepest section of the ACORK string, to clear constrictions in the hole and fill that may have accumulated at the bottom. This assembly was lowered to the seafloor, the hole was reentered, and the ACORK string was drilled into place (Fig. F9D). Once the target depth was reached, the packer inflation sequence was completed (Fig. F9E), the running tool was decoupled (Fig. F9F), a remotely operated vehicle (ROV) platform was lowered into place, and the drill string was recovered, leaving a fully installed ACORK (Fig. F9G).

Packers

The inflatable packers were constructed by TAM International, Inc., around standard-diameter, 8.48-m-long casing sections. The elements themselves consist of 3-m-long steel-reinforced (vertical stave), nitrile composition rubber bladders, rated to 100°C and effective to 140°C in this application. The elements are attached to the casing core at the

F9. ACORK installation stages, p. 38.



bottom of the packer and to a sealed sliding sleeve at the top. The sleeve rides on an annular volume through which the monitoring and packer inflation lines pass. The bladders are designed to expand from their initial diameter of 15 in to a maximum of 22 in. A differential inflation pressure of ~150 psi (1 MPa) is required to overcome the rigidity of the elements.

The bladders are filled with the ½-in inflation tube in the hydraulic umbilical. Flow is passed from the tube into a plenum that feeds both the continuation of the inflation line and the bladder of each packer through a pair of valves. The first valve is in an initially closed state, and opens when a critical pressure in the plenum (relative to the local annular pressure) is reached, at which point filling begins. This pressure is set with shear wires selected for each packer such that the inflation occurs in a desired sequence. We chose to inflate from bottom to top, assuming that the annulus would probably remain at near-hydrostatic conditions until a packer was inflated overhead. Attempting a different inflation sequence would cause uninflated packers to be trapped in confined intervals, which could inhibit inflation or cause hydrofracturing. Bottom-up inflation optimizes the chances for annular water to escape as packers are filled and for the packers to inflate in a hydrostatic environment.

The final inflation pressures are set by a second shear-wire valve that when activated locks in a closed position. No flow into or out of the packer can occur after this point. For the Leg 196 ACORKs, these valves were set to close when the internal pressure in the packer bladders rose to a total of 600 psi (4.1 MPa) relative to the local annular pressure (i.e., roughly 3 MPa above the pressure required to expand the packer itself), with the exception of the shallowest two packers at Site 1173, which were inflated to a lower total of 400 psi (2.75 MPa) to avoid fracturing the weaker formation at that level. The fracture limit, defined by a combination of the overburden, tensile strength, deviatoric stress, and fluid pressure, is difficult to assess with any confidence. The inflation values were believed to be a conservative compromise between the risks of fracturing (under conditions of high formation pressure and confined conditions in the hole annulus) and incomplete inflation.

The inflation procedure is done in stages, with line pressure (defined at the rig floor downstream of the circulation pumps) increased initially to a pressure between the first- and second-element filling valve activating pressures, then to a second pressure between the second and third, etc. Pressure is held long enough at each stage to allow sufficient flow through the ½-in inflation line to fill each packer. If the annular pressure is close to hydrostatic, the sequence proceeds as planned. If any of the packers becomes isolated in an overpressured zone by hole closure above, packer filling is delayed until the line pressure allows the differential across the opening valve (line pressure to annulus) to exceed the preset shear-wire threshold. Filling then proceeds until the bladder-to-annulus differential reaches the closing valve threshold. With this possible eventuality in mind, line pressure is increased and held at a level equivalent to lithostatic pressure for 30 min at the end of the filling sequence.

Screens

Hydrologic access to the formation was provided by 7.6-m-long screen filters on 11.24-m casing joints, manufactured by Houston Wellscreen, Inc. Sand is packed in a 2-cm annulus between the outside

of a solid section of 10³/₄-in casing and a screen formed of wire wrapped on radial webs. Hydraulic lines leading to deeper intervals pass straight through the filters. The sampling and/or monitoring line accessing each filter is terminated in a separate, smaller (2-cm OD × 1-m length) wire-wrapped screen located within the screened section. Carbolite, an aluminum oxide ceramic, was used for the filter fill, with a grain size of 400–600 μm, a porosity of ~30%, and a permeability of $\sim 2 \times 10^{-10}$ m². The screen was wound with 0.085-in wire with 0.10-in wire-to-wire spacing and provided an effective open cross section of 15%. The design was intended to provide good hydrologic communication to the formation, with maximum effective contact area and permeability, while preventing sediment from invading and clogging the sampling or monitoring lines. The risk of clogging during installation was further reduced by having the monitoring lines closed to prevent flow through the screens; the monitoring lines open by action of spool valves activated during the packer inflation, as described below.

Tubing

Transmission of pressure signals to the seafloor sensors was accomplished using thick-walled, 316-L stainless steel tubing of 1/4-in OD and 0.035-in wall thickness. One smaller diameter (1/8-in OD, 0.028-in wall thickness) line was provided for sampling fluids from screens in the décollement zone or stratigraphic equivalent of the décollement zone. All lines were laid in a gentle helical wind around the 1/2-in OD (0.049-in wall thickness) packer inflation line, then jacketed with polyurethane to form a single, robust umbilical, provided by Cabett Services, Inc. Connections were made during deployment between the umbilical and the tubes leading through or from each packer or screen. In intervening sections the umbilical was banded to the outside of the casing sections.

The tubing was chosen to satisfy a variety of requirements. The packer line diameter was chosen to allow individual packers to be filled in ~10–15 min at the typical line pressures applied. Monitoring lines were chosen on the basis of what was felt to be a reasonable compromise between capacitance and resistance. Capacitance and resistance of the formation (the inverse of the product of these being equivalent to the hydraulic diffusivity) are likely to be very high in parts of the sediment section. Hence, to transmit pressure variations with no distortion over a reasonable range of frequency requires the observation system to have very low resistance and capacitance. The quartz pressure sensors are essentially incompressible, and the compressibility of the thick-walled tubing can also be ignored. The water filling the tubing is the primary source of compliance. Reducing the internal diameter of the tubing is advantageous in that lesser amounts of water are required to flow in and out of the formation to transmit pressure signals, but only up to the point when the translation of fluid in the tube begins to feel the effects of the tube wall. Simple calculations suggest that the selected inside diameter is large relative to when frictional effects would be significant. Semidiurnal tidal signals of 10 kPa amplitude would result in a maximum displacement of only 4 mm in the longest tube installed (940 m). Ultimately, the limiting factor was the size that could safely be handled without fear of clogging with either fine sediment invading the screens and filters or grease and constrictions at the tube joints. Given the volume of water in the line to the deepest screen and the volume of water in the filter itself, the volumetric displacement required to transmit a 10-kPa signal is 0.2 cm³. Distributed over the surface of the

screened interval, the fluid displacement would be only 3×10^{-5} mm. The period at which signals would begin to suffer a phase lag would be far shorter than we are planning to monitor initially (10 min) or are capable of monitoring (10 s).

Once undisturbed monitoring proceeds for a few years, an attempt will be made to sample fluid from basement and from the décollement zone. It is anticipated that basement will be sufficiently permeable that sampling can be done using the ¼-in-OD (0.46-mm ID) monitoring line without significant perturbation of the pressure signal. This will not be the case in sedimentary units that have low permeability. To minimize the pressure perturbation and formation flux and to achieve a reasonable flow velocity up the décollement zone sampling tube, it was necessary to reduce the tube diameter. The ⅛-in-OD tubing used was felt to be a reasonable compromise for this first attempt at an ACORK installation in light of competing goals of minimizing handling difficulty and clogging risks while maximizing flow velocity for a given flux.

ACORK Head Physical Configuration

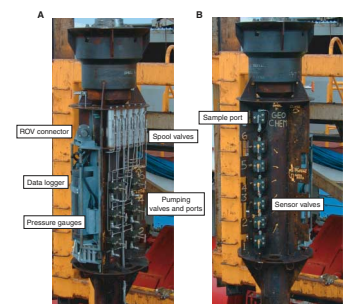
The ACORK head is a 30-in-diameter cylindrical frame fabricated from ⅜-in steel around a section of 11¾-in casing. It houses components in each of three 120°-wide, 60-in-high bays that are bounded above and below by circular horizontal bulkheads and divided from one another by radial webs (Fig. F10). The bays contain the following components described in more detail below: (1) the sensor/logger/underwater-mateable connector assembly on a demountable frame, (2) the spool valves and pumping/sampling valves and ports, and (3) the three-way pressure sensor valves and the geochemical sampling valve and port. The lowermost bulkhead is positioned ~16 in above the submersible landing platform that covers the reentry cone. Pairs of 3-in-OD, 2.75-in-ID docking tubes, 12 in center to center, are welded immediately beneath the lower bulkhead to provide an aid for maintaining submersible or ROV stability during site visits. Numerous cutouts on the vertical webs can be used as manipulator “hand holds” for the same purpose. At the top of the ACORK head is a 30-in reentry cone for drill-bit, subcasing, or wireline tool delivery systems.

Plumbing at the ACORK Head

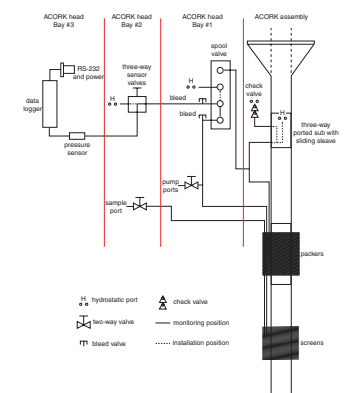
At the ACORK head, the packer, monitoring, and sampling lines are routed to several destinations (Fig. F11). The packer filling line is connected to a sliding sleeve valve contained within the ACORK running tool. During drilling-in operations and after completion of the installation, this valve routes the packer line to a check valve that prevents loss of line pressure but allows flow into the packers to prevent collapse during lowering. Drill pipe circulation is directed to the mud motor at the bottom of the ACORK assembly. After the hole is reamed and the assembly has reached the target depth, a wireline retrievable tool (“go-devil”) is used to shift the sleeve valve to a second position that diverts drill string pressure and flow from the mud-motor to the packer inflation line. At this point the stepwise sequence of packer inflation begins.

Another branch of the packer inflation line leads from the sliding sleeve valve to a manifold that passes the packer inflation line pressure to a bank of locking spool valves, one for each screen. Two positions of the spool valves, controlled by the packer line pressure, provide two different routings among screen lines, pressure sensor lines, and a local

F10. ACORK instrument bays, p. 45.



F11. ACORK plumbing schematic, p. 46.



hydrostatic port. During deployment, drilling, and packer filling operations, lines from the screens are closed and lines from the pressure sensors are routed to a local hydrostatic port. Venting the sensor lines prevents damage to pressure sensors from any excess pressures that might be produced during drilling and packer inflation, and allows a local hydrostatic calibration point to be established before the sensors are connected to the monitoring lines. Keeping the screen lines closed prohibits flow through the screens and minimizes the potential for infiltration of fine-grained material into the sand-packed screens. The spool valves are set to shift when the packer inflation line pressure reaches 1800 psi (12.4 MPa) (i.e., once all packers are inflated). Once they shift and lock, the spool valves close the hydrostatic port and interconnect the screen and pressure sensor lines for monitoring. The spool valves are designed to shift with no volumetric change so that no pressure pulse is generated that could potentially damage the pressure sensors.

A manual means for pressure sensor protection and calibration is provided by three-way valves plumbed into the pressure sensor lines downstream from the valved pumping and sampling ports described below. In their normal position, pressure from the screens (via the spool valves) is routed directly to the pressure sensors. In the second position, the sensor lines are opened to hydrostatic pressure and the screen lines are closed. Thus, these serve the same function as the spool valves but with manual control. The sensors can be isolated temporarily if pumping experiments are ever performed, hydrostatic reference checks can be done at the time of any submersible or ROV visit, and the screen lines can be closed to prevent drainage of the formation if the logger/sensor unit is ever removed.

Above the three-way valves (further downstream from the screens), the monitoring lines are routed to the pressure sensors via underwater-mateable couplers mounted at the base of the framework holding the data logger and pressure sensors. The sliding-sleeve couplers are pressure balanced so that the line pressures are radial only. No piston force is generated under conditions of high screen-line pressure. The down-hole ends of the couplers are closed by spring-loaded sleeves when they are unmated, and thus provide additional safety against leakage if the logger unit is ever removed.

In addition to the lines leading from the screens to the spool valves and onto the pressure sensors, there are also lines leading to valved pumping/sampling ports where fluid samples can be collected and pumping tests performed. In the Nankai Trough ACORKs, one is a devoted geochemical sampling port connected to the small-diameter line that leads directly to its own rolled-screen manifold in the décollement zone screen. Other pumping/sampling ports lead from local "T" junctions in the monitoring lines. If any pumping tests are ever carried out in the future, the three-way pressure sensor isolation valves would need to be switched to protect the sensors.

A critical step in the assembly operation is to purge air from all lines. In quantities too large to be absorbed by the local volume of water, trapped air will greatly increase the compressibility of the system and thus reduce the fidelity of the response to high-frequency formation pressure variations. The packers are filled with water at the moonpool immediately before they are deployed, and the packer line is purged via the check valve in the running tool. The monitoring lines in the umbilical are purged through manually closed ports at the spool valves, and the lines running from the spool valves to the pressure sensors are pre-charged with water.

Pressure Sensors and Electronics

Pressure sensors and data loggers (Figs. F10, F11) are housed in frames that can be lifted from the ACORK heads in the event that service of any of the components is required. This monolithic subassembly weighs 115 kg in water, and includes the data logger in its pressure case, multiple pressure sensors connected to the monitoring lines and one for monitoring seafloor pressure variations, an eight-pin underwater-mateable electrical connector, and interconnecting cables. The frames are supported on four pins mated into tapered-throat sockets welded to the ACORK head. O-rings and a valved hydraulic line on the upper pair provide a hydraulic lock for deployment, and allow the frame to be pumped from its mount in the ACORK head if necessary. The valve and hydraulic coupler are mounted to the ACORK head directly above the data logger bay (Fig. F10).

The pressure sensors, manufactured by Paroscientific, Inc., employ matched pairs of quartz crystals. Line or hydrostatic pressure is applied to one via a Bourdon tube, and the other is isolated from stress to provide temperature compensation. Pressure is calculated on the basis of the resonant frequency of the loaded quartz crystal (with temperature effects determined from the second crystal removed). The total range of the sensors used during Leg 196 is 70 MPa (7000 m equivalent water depth). Data are logged as 24-bit values; the actual pressure resolution realized is dependent upon the time over which the frequency was determined (determined as the time-integrated cycle counts), which in turn affects the power consumption. The integration time used (0.7 s) provides a resolution of $\sim 10^{-6}$ of full scale, or 70 Pa. Absolute accuracy is limited by sensor calibration and drift. Experience from previous multi-year deployments shows that drift is typically <0.4 kPa/yr. This and calibration inaccuracy ($\sim 5 \times 10^{-4}$ of total pressure or 25 kPa at the Nankai Trough sites) are dealt with well by the intergauge hydrostatic checks both prior to final installation and later at times of submersible visits.

Sensors are activated at a user-specified interval and data are recorded with a logger built by Richard Brancker Research, Ltd. The logger is controlled by a Zilog Z80S153 processor and has modular capability to store up to 32 channels of pressure and temperature. Time-tagged pressure data are recorded in 8-MB-capacity flash memory. Logging rates are programmable at sampling intervals ranging from 10 s to 1 day. With seven gauges being logged at 10-min intervals at Site 808, memory capacity will provide 3 yr of operation. Power is supplied by lithium sulfurylchloride battery packs at 7.4 V with a capacity of 360 A·hr, sufficient at this rate of logging for more than the shelf life of the batteries (15 yr). Logging can be extended beyond the life of the batteries by applying power from an external source through the underwater-mateable connector.

CORE PHYSICAL PROPERTIES

The multisensor track (MST) was run for nondestructive measurements of wet bulk density, magnetic susceptibility, and natural gamma radiation on whole-round cores. Two whole-round samples were then taken for postcruise in situ permeability and physical properties measurements. After the samples were split and labeled, minicore samples were cut for moisture and density and *P*-wave velocity measurements.

Thermal conductivity measurements using the half-space method were made on the archive-half sections. A detailed description of the techniques used is given in the ODP Physical Properties Handbook (Blum, 1997) and is only summarized here.

Multisensor Track

The MST combines four sensors on an automated track to measure magnetic susceptibility, bulk density, *P*-wave velocity, and natural gamma ray emission on whole-core sections. *P*-wave velocity was not collected because of the incomplete coupling between the liner and the core.

Magnetic Susceptibility

Magnetic susceptibility was measured with a Bartington MS2 meter using an 80-mm internal diameter sensor loop (88-mm coil diameter) operating at a frequency of 565 Hz and an alternating field of 80 A/m (0.1 mT). The sensitivity range was set to the low sensitivity setting (1.0 Hz). The sampling interval was set to 2 cm. The quality of these results is degraded because samples were fragmented into 3- to 10-cm-sized pieces. Nevertheless, general trends are useful for the overview of the variability in basalt composition. The measured magnetic susceptibilities are relative and have not been corrected for differences between core and coil diameters.

Gamma Ray Attenuation

Bulk density was estimated for whole-round core sections as they passed through the gamma ray attenuation (GRA) bulk densiometer with a sampling period and interval of 2 s and 10 cm, respectively. The gamma ray source was ¹³⁷Cs. Since bulk densities are estimated by measuring the attenuation of gamma rays that pass through the core, a constant sample thickness is required. However, most samples were fragmented into 3- to 10-cm-sized pieces, which degraded the quality given the 10-cm sampling interval. Therefore, results can only be used for general trends.

Natural Gamma Radiation

Natural gamma radiation (NGR) analysis is a function of the random and discrete decay of radioactive atoms and is measured through scintillating detectors as outlined by Hoppie et al. (1994). During Leg 196, NGR emissions were measured for 20 s at 10-cm intervals. NGR calibration was performed at the beginning of the leg.

Moisture and Density

Bulk density, grain density, and porosity were calculated from measurements of wet and dry masses and dry volumes (Method C of Blum, 1997). Eleven ~10-cm³ samples were taken from split cores. Sample mass was determined using a Scientech electronic balance. The sample mass was counterbalanced by a known mass of 20 g so that only mass differences of usually <2 g were measured. The balance was also equipped with a computer-averaging system that corrected for ship accelerations. Dry mass was measured from samples that were oven-dried

at $110^{\circ} \pm 5^{\circ}\text{C}$ for 24 hr and cooled in a desiccator for 2 hr. Dry volumes were determined using a helium-displacement Quantachrome Penta-Pycnometer. Sample volume measurements were repeated up to five times until the last set of measurements had a standard deviation $<0.01\%$. A purge time of 1 min was used before each run. A reference sphere of known volume was run with each group of four samples during all measurements. The standard was rotated systematically among cells to check for errors.

***P*-wave Velocity**

P-wave velocity was measured on basalt minicore samples using the PWL3 modified Hamilton Frame velocimeter (Boyce, 1976). The PWS3 contact probe system measures the traveltime of a 500-kHz signal through a sample, with the oriented sample (cube) placed directly between the transducers in the desired orientation (x-, y-, and z-direction; these directions are defined in Blum, 1997). The minicore samples had their sides cut with the parallel saw so that all three orientations could be measured. Sample thickness was measured directly by a digital caliper. The velocity data recorded in the Janus database are uncorrected for in situ temperature and pressure (such corrections can be made using the relationships in Wyllie et al., 1956).

Calibration of the system was performed according to Blum (1997). The separation between transducers was calibrated with four polycarbon standards with varying thickness (20–50 mm). The delay time was determined by a linear regression of traveltime vs. thickness (15.4–57.5 mm) of seawater. An external digital thermometer was used to record core temperature. The values were stored in the database but were not used in this report.

Anisotropy was calculated using the following equation:

$$\text{Anisotropy (\%)} = (V_{pt} - V_{pl}) / [(V_{pt} + V_{pl}) / 2] \times 100,$$

where V_{pt} is the transverse (z-oriented) *P*-wave velocity and V_{pl} is the longitudinal velocity. V_{pl} was determined as the average *P*-wave velocity in the x- and y-directions.

Thermal Conductivity

Thermal conductivity is the measure of a material's ability to transmit heat by molecular conduction and is required for heat flow determinations.

The TK04 system (Teka, Berlin) was used for thermal conductivity measurements. For basalt samples, a smooth surface was prepared on ~6-cm-long split-core specimens that had been placed in a seawater-filled bath until they were resaturated with seawater and thermally equilibrated. The half-space needle probe (#H19608) was secured onto the flat surface of the split core. The needle probe (1.9-mm diameter \times 70-mm length) contains a heater wire and a calibrated thermistor.

At the beginning of each half-space measurement, temperatures in the samples were monitored automatically, without applying a heater current, until the background thermal drift was determined to be $<0.04^{\circ}\text{C}/\text{min}$. The heater circuit was then closed and the temperature increase in the probe was recorded.

The reported thermal conductivity value for each sample is the average of four repeated measurements. Thermal conductivities were calcu-

lated from the rate of temperature rise while the heater current was flowing. Temperatures measured during the first 80 s of the heating cycle were fitted to an approximate solution of a constantly heated line source (Kristiansen, 1982; see Blum [1997] for details). Data are reported in W/(m·K) with a stated error of 5%–10%. The choices of measurement interval and assessment of thermal stability are automatic with the TK04 meter, which does not require shipboard calibration. Table T4 gives thermal conductivity measurements for two standard samples, Macor and red rubber. Other “legacy” standards (black rubber, 504B basalt, and fused silica) could not be found on the ship, which prevented construction of a calibration line for the half-space probes. However, measured values for Macor, which are close to basalt conductivities, match reported values very well. Thus we did not apply any further calibration afterwards. Also, corrections were not attempted for in situ temperature or pressure effects.

T4. Thermal conductivities of half-space standards, p. 51.

IGNEOUS PETROLOGY AND VOLCANOLOGY³

Core Curation and Shipboard Sampling

To describe important mineralogic and structural features we examined both the archive and working halves of core sections containing igneous rocks. Each piece was numbered sequentially from the top of each core section and labeled on the outside surface. Pieces that could be fitted together were assigned the same number and were lettered consecutively (e.g., 1A, 1B, 1C, etc.). Plastic spacers were placed between pieces with different numbers. The presence of a spacer may represent a substantial interval of no recovery. If it was evident that an individual piece had not rotated about a horizontal axis during drilling, an arrow was added pointing toward the top of the section.

Nondestructive physical properties measurements, such as color imaging and natural gamma ray emission, were made on the core before it was split (see “Core Physical Properties,” p. 18). After the core was split, lithologic descriptions were made of the archive half. The working half was sampled for shipboard physical properties measurements (see “Core Physical Properties,” p. 18), magnetic studies (see “Paleomagnetism and Rock Magnetism,” p. 25), thin section analysis, and X-ray diffraction and inductively coupled plasma–atomic emission spectrometry (ICP-AES) analyses. The archive halves were described on visual core description (VCD) forms and photographed.

Visual Core Descriptions

We used VCD forms to document each section of the igneous rock cores. The left column on the form, adjacent to the core photograph, represents the archive half. A horizontal line across the entire width of the column denotes a plastic spacer. Oriented pieces are indicated on the form by an upward-pointing arrow to the right of the piece. A description of the symbols, colors, and other notations used on the VCDs is provided in Figure F12.

Locations of samples selected for shipboard studies are indicated in the “Shipboard studies” column with the following notation: ICP = ICP-AES analysis, TSB = petrographic thin section, PP = physical properties measurements, and PMAG = paleomagnetic measurements.

F12. Igneous texture and structure definitions, p. 47.

Alteration	V	F	S	M	B	V	C
	None	Fracture	Slight	Moderate	High	Very High	Complete
Granularity	P	A	C	M	F	M	C
	Phenocrystalline (100-500 μm)	Aphanitic	Coarse grained (1-5 mm)	Medium grained (1-2 mm)	Fine grained (0.5-1.0 mm)	Microcrystalline (0.1-1 mm)	Crystalline crystalline
Groundmass Crystallinity	C	H	S	H	F	G	
	Hypocrystalline (50-100 μm crystals)	Hypocrystalline (20-40 μm crystals)	Hypocrystalline (10-20 μm crystals)	Hypocrystalline (5-10 μm crystals)	Hypocrystalline (2-5 μm crystals)	Glass	
Boundary	---	---	---	---	---	---	---
	Lobe boundary	Lobe boundary?	Lobe contact	Lobe contact?	Lobe contact?	Lobe contact?	Lobe contact?

³This section was written during Leg 197. See Leg 197 Contributors for addresses.

Structural features are noted in the “Volcanology/Structure” column and include vesicularity, where NV = nonvesicular (vesicle content <1%), SV = sparsely vesicular (vesicle content = 1%–5%), MV = moderately vesicular (vesicle content = 5%–20%), HV = highly vesicular (vesicle content >20%), G = unaltered glass, and (G) = altered glass.

The “Alteration” column is used to denote the presence of veins (V).

We determined that the hard rock cores contained only one lithologic unit, on the basis of similar color, structure, brecciation, grain size, vesicle abundance, mineral occurrence, and abundance. Written descriptions accompany the schematic representation of the core sections, and include the following:

1. The leg, hole, core, core type, and section number (e.g., 196-1173A-15R-3), as well as the top of the core section measured in meters below seafloor.
2. The unit number (consecutive downhole), rock name, and piece numbers. We assigned provisional rock names on the basis of hand specimen observation (using a hand lens and binocular microscope) and later checked these assignments by examining thin sections. Porphyritic rocks were named by phenocryst type, where the term “phenocryst” was used for a crystal that was significantly (typically five times) larger than the average size of the groundmass crystals and/or generally euhedral in shape. Phenocryst abundance descriptors were further modified by including the names of phenocryst phases, in order of decreasing abundance. Thus, a “moderately plagioclase-olivine-phyric basalt” contains >10% (by volume) phenocrysts, the dominant phenocryst being olivine, with lesser amounts of plagioclase. As long as the total content >1%, the minerals named include all of the phenocryst phases that occur in the rock.
3. Contact relations and unit boundaries. After we made lithologic descriptions, we attempted to integrate the observations to define unit boundaries. The boundaries often reflect major physical changes in the core (e.g., pillowed vs. massive) that were also observed in the physical properties and downhole measurements. Intervals of sediment and/or hyaloclastite, changes in vesicularity, alteration, volume fraction, and type of matrix also define lithologic contacts. Where possible, whole-rock ICP-AES analyses (see “[ICP-AES Analysis](#),” p. 23) were used to investigate chemical differences between units. Note that, whereas every effort was made to have unit boundaries reflect individual lava packages, the term “unit” should not necessarily be considered synonymous with “lava flow” in this volume.
4. Phenocrysts. This entry describes the types of minerals visible with a hand lens or binocular microscope, their distribution within the unit, and, for each phase, its abundance (volume percent), size range (millimeters), shape, and degree of alteration, with further comments if appropriate.
5. Groundmass texture and grain size, where the grain-size categories used are glassy, aphanitic, fine grained (<1 mm), medium grained (1–5 mm), or coarse grained (>5 mm). Changes in grain size and proportions of crystals and glass within units were also noted.
6. Vesicles. This entry records vesicle abundance (visual estimates of the volume fraction of vesicles were supplemented by observations using a binocular microscope), size, shape (sphericity

- and angularity), and whether the vesicles are empty or filled and the nature of the filling.
7. Color name and code (for the dry rock surface) according to the Munsell rock color charts (Rock-Color Chart Committee, 1991).
 8. Structure. This entry refers to whether the unit is massive, pillowed, hyaloclastic, banded, brecciated, scoriaceous, or tuffaceous. We sought to produce an integrated picture of the style of volcanism and environmental setting of the drill site by identifying features that are diagnostic of specific physical processes. Pillowed sequences were inferred using the presence of glassy margins and/or groundmass grain-size variations. A section was described as massive if there was no evidence for pillows, even though it may be part of a pillowed sequence. The interpretation of the lavas involved three steps: (1) the observed features were tied to physical processes, (2) the emplacement style of individual flows was inferred, and (3) the environmental setting (e.g., subaerial or submarine) for the whole sequence was discussed.
 9. Alteration. We graded the degree of alteration as unaltered (<2% of alteration products by volume), slight (2%–10%), moderate (10%–40%), high (40%–80%), very high (80%–95%), or complete (95%–100%). Changes of alteration through a section or a unit were also noted. Where possible, we identified the secondary minerals as carbonate, clay, zeolite, or iron oxide.
 10. Veins and fractures. We described their abundance, width, orientation, and mineral linings and fillings. Locations of veins were indicated by V on the VCDs. The minerals filling the veins were identified as in the “Alteration” portion of the VCDs.
 11. Any additional comments.

Thin Section Descriptions

We examined thin sections from the core intervals noted on the VCD forms to complement and refine the hand-specimen observations. In general, the same terminology was used for thin section descriptions as for the VCDs. The percentages of individual phenocryst, groundmass, and alteration phases were estimated visually, and textural descriptions were reported (see “[Site 1173 Thin Sections](#),” p. 6). The textural terms used are defined by MacKenzie et al. (1982). For some porphyritic basalts, the thin section and visual core descriptions may differ slightly, typically because small plagioclase laths in a rock with seriate texture are visible only in thin section. Thus, a rock described visually as olivine-plagioclase-phyric may be described as plagioclase-olivine-phyric in the thin section description.

ICP-AES Analysis

We selected representative samples of major lithologic units for shipboard ICP-AES analysis. Large whole-rock pieces were first cut with a diamond-impregnated saw blade and ground on a diamond wheel to remove surface contamination. Samples were washed in an ultrasonic bath containing methanol for ~10 min, followed by three consecutive ~10-min washes in an ultrasonic bath containing nanopure deionized water, and then dried for ~12 hr in an oven at 110°C. The cleaned whole-rock samples (~20 cm³) were reduced to fragments <1 cm in diameter by crushing between two disks of Delrin plastic in a hydraulic press, and ground for ~5 min in a Spex 8510 shatterbox with a tungsten

carbide barrel. The sample powders were weighed on a Scientech balance, and ignited to determine weight loss on ignition.

We weighed 0.100 ± 0.002 g aliquots of the ignited whole-rock powders and mixed them with 0.4000 ± 0.0004 g of Li-metaborate (LiBO_2) flux that had been preweighed on shore. Standard rock powders and full procedural blanks were included with the unknowns for each sample run. All samples and standards were weighed on the Cahn Electro balance. Weighing errors are conservatively estimated to be ± 0.00001 g.

Mixtures of flux and rock powders were fused in Pt-Au crucibles at 1050°C for 10–12 min in a Bead Sampler NT-2100. Ten microliters of 0.172-mM aqueous lithium bromide (LiBr) solution was added to the mixture before fusion, as an anti-wetting agent to prevent the cooled bead from sticking to the crucible. Cooled beads were transferred to 125-mL polypropylene bottles and dissolved in 50 mL of 2.3-M HNO_3 by shaking with a Burrell Wrist Action bottle-shaker for an hour. After digestion of the glass bead, all of the solution was filtered to 0.45 microns into a clean 60-mL wide-mouth polypropylene bottle. Next, 2.5 mL of this solution was transferred to a plastic vial and diluted with 17.5 mL of 2.3-M HNO_3 to bring the total volume to 20 mL. The solution-to-sample dilution factor for this procedure is ~ 4000 . Dilutions were conducted using a Brinkman dispensette (0–25 mL).

Major (Si, Ti, Al, Fe, Mn, Mg, Ca, Na, K, and P) and trace (Zr, Y, Nb, Sr, Ba, Ni, Cr, Sc, V, Co, Cu, and Zn) element concentrations of powder samples were determined with the JY2000 ULTRACE ICP-AES. The JY2000 sequentially measures characteristic emission intensities (with wavelengths between ~ 100 and 800 nm). ICP-AES protocols for dissolution and analysis of rock powders were developed by Murray et al. (2000) (see also Shipboard Scientific Party, 2001). The elements analyzed, emission lines used, and the specific analytical conditions for each sample are provided in Table T5.

The JY2000 plasma was ignited 30 min before each run to allow the instrument to warm up and stabilize. After the warm-up period, a zero-order search was performed to check the mechanical zero of the diffraction grating. After the zero-order search, the mechanical step positions of emission lines were tuned by automatically searching with a 0.002-nm window across each emission peak using the University of Massachusetts Kilauea basalt laboratory standard K-1919, prepared in 2.3-M HNO_3 . The only exception is P, which was automatically searched for using a single element standard. During the initial setup, an emission profile was collected for each peak, using K-1919, to determine peak-to-background intensities and to set the locations of background points for each element. The JY2000 software uses these background locations to calculate the net intensity for each emission line. The photomultiplier voltage was optimized by automatically adjusting the gain for each element using the standard (BHVO-2, JB-1a, BIR-1, or K1919) with the highest concentration for that element. Before each run, a profile of K-1919 was collected to assess the performance of the machine from day to day. A typical sample run lasted ~ 12 –14 hr, depending on the number of samples and replicate analyses.

All ICP-AES data presented in the site report were acquired using Mode 2 of the JY2000 software, except for Fe, Mg, Mn, Ba, Cr, Sc, V, and Y data, which were acquired in Mode 5. In Mode 5, the intensity at the peak of an emission line is measured and averaged over a given counting interval repeated three times sequentially. Mode 2 fits a Gaussian curve to a variable number of points across a peak and then integrates

T5. ICP-AES parameters, p. 52.

to determine the area under the curve. The parameters for each run are given in Table T5. Each unknown sample was run at least twice, nonsequentially, in all sample runs.

A typical ICP-AES run includes (1) a set of three certified rock standards (BHVO-2, BIR-1, and JB-1a; Table T6) run at the beginning, middle, and end of the sample run; (2) up to 11 unknown samples; (3) a drift-correcting sample (the K-1919 standard) analyzed every fourth sample position; and (4) a blank solution run near the beginning, middle, and end of each run. A 2.3-M HNO₃ wash solution was run for a minimum of 90 s between each of the samples and standards.

Following each sample run, the raw intensities were transferred to a data file and data reduction was completed using a spreadsheet to ensure proper control over standardization and drift correction. Once transferred, intensities for all samples were corrected for the full procedural blank. A drift correction was then applied to each element by linear interpolation between drift-monitoring solutions run before and after a particular batch of samples. The interpolation was calculated using the lever rule. Following blank subtraction and drift correction, concentrations for each sample were calculated from the average intensity per unit concentration for the standard BHVO-2, which was analyzed twice during the run.

Estimates of accuracy and precision for major and trace element analyses were based on replicate analyses of BHVO-2, BIR-1, and JB-1a, the results of which are presented in Table T6. In general, run-to-run relative precision by ICP-AES was better than 2% for the major elements. Run-to-run relative precision for trace elements was generally <5%. Exceptions typically occurred when the element in question was near the detection limit of the instrument (see Table T5 for machine detection limits).

PALEOMAGNETISM AND ROCK MAGNETISM⁴

Paleomagnetic investigations of Leg 196 Hole 1173B cores conducted during Leg 197 consisted of measurements of natural remanent magnetization, stepwise alternating-field (AF) demagnetizations and subsequent remanence measurements, and measurements of bulk magnetic susceptibility. The remanence of oriented discrete samples from the working-half sections was primarily measured using a 2G Enterprises DC-Superconducting Quantum Interference Device (SQUID) magnetometer (Model 760R). The 2G SQUID magnetometer is equipped with an in-line AF demagnetizer (Model 2G600), which can demagnetize samples to peak fields of 80 mT. Both the magnetometer and AF demagnetizer are interfaced with a PC-compatible computer and are controlled by 2G's Long Core software (National Instruments). Some discrete samples were also measured using a Molspin Minispin spinner magnetometer. A DTECH D-2000 AF demagnetizer was available for stepwise demagnetization of those discrete samples measured with the Molspin magnetometer. The DTECH demagnetizer is capable of peak fields up to 200 mT. Bulk magnetic susceptibilities for discrete samples were measured using a Geofyzika Brno Kappabridge KLY-2 magnetic susceptibility meter. Calibrations of these instruments were based on shipboard standards and standards from the University of Rochester.

The standard ODP core orientation convention (fig. 8 in Shipboard Scientific Party, 1991a; fig. 8 in Shipboard Scientific Party, 1997) was applied. The convention is such that the +z-axis of the sample is parallel

T6. ICP-AES values of reference standards, p. 53.

⁴This section was written during Leg 197. See Leg 197 Contributors for addresses.

downhole to the z-axis of the drill core. With the split face of the drill core representing the y-z plane, the x-axis is then perpendicular to the split face and is directed into the working half of the core. The x-axis is used as the reference “geomagnetic” north for the definition of magnetic declination values. Discrete minicores were marked with an arrow in the -z-axis (uphole) direction on the plane representing the split surface of the working half.

Discrete samples were taken from basalt rocks by drilling cylindrical minicores (~10 cm³) with a water-cooled drill bit attached to a standard drill press. Minicores were oriented following the convention discussed above.

REFERENCES

- Anadrill-Schlumberger, 1993. *Logging While Drilling*: Houston (Schlumberger), document SMP-9160.
- Austin, J.A., Jr., Christie-Blick, N., Malone, M.J., et al., 1998. *Proc. ODP, Init. Repts.*, 174A [CD-ROM]. Available from: Ocean Drilling Program, Texas A&M University, College Station TX 77845-9547, U.S.A.
- Bangs, N.L., Taira, A., Kuramoto, S., Shipley, T.H., Moore, G.F., Mochizuki, K., Gulick, S.S., Zhao, Z., Nakamura, Y., Park, J.-O., Taylor, B.L., Morita, S., Ito, S., Hills, D.J., Leslie, S.C., Alex, C.M., McCutcheon, A.J., Ike, T., Yagi, H., and Toyama, G., 1999. U.S.-Japan collaborative 3-D seismic investigation of the Nankai Trough plate-boundary interface and shallowmost seismogenic zone. *Eos*, 80:569.
- Becker, K., Bartetzko, A., and Davis, E.E., 2001. Leg 174B synopsis: revisiting Hole 395A for logging and long-term monitoring of off-axis hydrothermal processes in young oceanic crust. In Becker, K., and Malone, M.J. (Eds.), *Proc. ODP, Sci. Results*, 174B, 1–12 [CD-ROM]. Available from: Ocean Drilling Program, Texas A&M University, College Station TX 77845-9547, USA.
- Becker, K., and Davis, E.E., 1998. Advanced CORKs for the 21st Century. *JOI/USSSP-sponsored workshop report* [Online]. Available from World Wide Web: <http://www.joiscience.org/USSSP/Workshops/AdvancedCORKs/Advanced_CORK_report.html>. [Cited 2001-05-02]
- , 2000. Plugging the seafloor with CORKs. *Oceanus*, 42:14–16.
- Becker, K., Fisher, A.T., and Davis, E.E., 1997. The CORK experiment in Hole 949C: long-term observations of pressure and temperature in the Barbados accretionary prism. In Shipley, T.H., Ogawa, Y., Blum, P., and Bahr, J.M. (Eds.), *Proc. ODP, Sci. Results*, 156: College Station, TX (Ocean Drilling Program), 247–252.
- Binns, R.A., Barriga, F.J.A.S., Miller, D.J., et al., 2002. *Proc. ODP, Init. Repts.*, 193 [CD-ROM]. Available from Ocean Drilling Program, Texas A&M University, College Station TX 77845-9547, USA.
- Blum, P., 1997. Physical properties handbook: a guide to the shipboard measurements of physical properties of deep-sea cores. *ODP Tech. Note*, 26 [Online]. Available from World Wide Web: <<http://www-odp.tamu.edu/publications/tnotes/tn26/INDEX.HTM>>. [Cited 2001-05-02]
- Boyce, R.E., 1976. Definitions and laboratory techniques of compressional sound velocity parameters and wet-water content, wet-bulk density, and porosity parameters by gravimetric and gamma-ray attenuation techniques. In Schlanger, S.O., Jackson, E.D., et al., *Init. Repts. DSDP*, 33: Washington (U.S. Govt. Printing Office), 931–958.
- Davis, E.E., and Becker, K., 1993. Studying crustal fluid flow with ODP borehole observatories. *Oceanus*, 36:82–86.
- , 1994. Formation temperatures and pressures in a sedimented rift hydrothermal system: ten months of CORK observations, Holes 857D and 858G. In Mottl, M.J., Davis, E.E., Fisher, A.T., and Slack, J.F. (Eds.), *Proc. ODP, Sci. Results*, 139: College Station, TX (Ocean Drilling Program), 649–666.
- , 1998. Borehole observatories record driving forces for 374 hydrothermal circulation in young oceanic crust. *Eos*, 79:369.
- , 1999. Tidal pumping of fluids within and from the oceanic crust: new observations and opportunities for sampling the crustal hydrosphere. *Earth Planet. Sci. Lett.*, 172:141–149.
- Davis, E.E., Becker, K., Pettigrew, T., Carson, B., and MacDonald, R., 1992. CORK: a hydrologic seal and downhole observatory for deep-ocean boreholes. In Davis, E.E., Mottl, M.J., Fisher, A.T., et al., *Proc. ODP, Init. Repts.*, 139: College Station, TX (Ocean Drilling Program), 43–53.
- Davis, E.E., Becker, K., Wang, K., and Carson, B., 1995. Long-term observations of pressure and temperature in Hole 892B, Cascadia accretionary prism. In Carson, B.,

- Westbrook, G.K., Musgrave, R.J., and Suess, E. (Eds.). *Proc. ODP, Sci. Results*, 146 (Pt. 1): College Station, TX (Ocean Drilling Program), 299–311.
- Davis, E.E., Wang, K., Becker, K., and Thomson, R.E., 2000. Formation-scale hydraulic and mechanical properties of oceanic crust inferred from pore-pressure response to periodic seafloor loading. *J. Geophys. Res.*, 105:13423–13435.
- Davis, J.C., 1973. *Statistics and Data Analysis in Geology*: New York (Wiley).
- Foucher, J.-P., Henry, P., and Harmegnies, F., 1997. Long-term observations of pressure and temperature in Hole 948D, Barbados accretionary prism. *In* Shipley, T.H., Ogawa, Y., Blum, P., and Bahr, J.M. (Eds.), *Proc. ODP, Sci. Results.*, 156: College Station, TX (Ocean Drilling Program), 239–245.
- Hills, D.J., Moore, G.F., Bangs, N.L., Gulick, S.S., and Leg 196 Shipboard Scientific Party, 2001. Preliminary results from integration of 2D PSDM and ODP Leg 196 LWD velocity data in the Nankai accretionary prism. *Eos, Trans., Am. Geophys. Union*, 82:F1221.
- Hoppie, B.W., Blum, P., and the Shipboard Scientific Party, 1994. Natural gamma-ray measurements on ODP cores: introduction to procedures with examples from Leg 150. *In* Mountain, G.S., Miller, K.G., Blum, P., et al., *Proc. ODP, Init. Repts.*, 150: College Station, TX (Ocean Drilling Program), 51–59.
- Kimura, G., Silver, E.A., Blum, P., et al., 1997. *Proc. ODP, Init. Repts.*, 170: College Station, TX (Ocean Drilling Program).
- Kristiansen, J.I., 1982. The transient cylindrical probe method for determination of thermal parameters of earth materials [Ph.D. dissert.]. Aarhus Univ.
- MacKenzie, W.S., Donaldson, C.H., and Guilford, C., 1982. *Atlas of Igneous Rocks and their Textures*: Harlow, England (Longman).
- Moore, G.F., Taira, A., Bangs, N.L., Kuramoto, S., Shipley, T.H., Alex, C.M., Gulick, S.S., Hills, D.J., Ike, T., Ito, S., Leslie, S.C., McCutcheon, A.J., Mochizuki, K., Morita, S., Nakamura, Y., Park, J.-O., Taylor, B.L., Toyama, G., Yagi, H., and Zhao, Z., 2001. Data report: Structural setting of the Leg 190 Muroto transect. *In* Moore, G.F., Taira, A., Klaus, A., et al., *Proc. ODP, Init. Repts.*, 190, 1–14 [CD-ROM]. Available from: Ocean Drilling Program, Texas A&M University, College Station TX 77845-9547, USA.
- Moore, J.C., and Klaus, A. (Eds.), 2000. *Proc. ODP, Sci. Results*, 171A [CD-ROM]. Available from: Ocean Drilling Program, Texas A&M University, College Station TX 77845-9547, USA.
- Moore, J.C., Klaus, A., et al., 1998. *Proc. ODP, Init. Repts.*, 171A: College Station, TX (Ocean Drilling Program).
- Murray, R.W., Miller, D.J., and Kryc, K.A., 2000. Analysis of major and trace elements in rocks, sediments, and interstitial waters by inductively coupled plasma-atomic emission spectrometry (ICP-AES). *ODP Tech. Note*, 29 [Online]. Available from World Wide Web: <<http://www-odp.tamu.edu/publications/tnotes/tn29/INDEX.HTM>>. [Cited 2001-05-02]
- O'Brien, P.E., Cooper, A.K., Richter, C., et al., 2001. *Proc. ODP, Init. Repts.*, 188 [CD-ROM]. Available from: Ocean Drilling Program, Texas A&M University, College Station TX 77845-9547, USA.
- Rock-Color Chart Committee, 1991. *Rock Color Charts*. Geol. Soc. Am.
- Salisbury, M.H., Shinohara, M., Richter, C., et al., 2002. *Proc. ODP, Init. Repts.*, 195 [CD-ROM]. Available from: Ocean Drilling Program, Texas A&M University, College Station TX 77845-9547, USA.
- Schlumberger, 1989. *Log Interpretation Principles/Applications*: Houston (Schlumberger Educ. Services), SMP-7017.
- Schlumberger, 1994. *Log Interpretation Charts*: Sugar Land (Schlumberger), SMP-7006.
- Screaton, E.J., Carson, B., and Lennon, G.P., 1995. Hydrogeologic properties of a thrust fault within the Oregon accretionary prism. *J. Geophys. Res.*, 100:20025–20035.

- Screaton, E.J., Fisher, A.T., Carson, B., and Becker, K., 1997. Barbados Ridge hydrogeologic tests: implications for fluid migration along an active decollement. *Geology*, 25:239–242.
- Serra, O., 1986. *Fundamentals of Well-Log Interpretation (Vol. 2): The Interpretation of Logging Data*. Dev. Pet. Sci., 15B.
- Shipboard Scientific Party, 1991a. Explanatory notes. In Davies, P.J., McKenzie, J.A., Palmer-Julson, A., et al., *Proc. ODP, Init. Repts.*, 133 (Pt. 1): College Station, TX (Ocean Drilling Program), 31–58.
- , 1991b. Site 808. In Taira, A., Hill, I., Firth, J.V., et al., *Proc. ODP, Init. Repts.*, 131: College Station, TX (Ocean Drilling Program), 71–269.
- , 1992. Explanatory notes. In Davis, E.E., Mottl, M.J., Fisher, A.T., et al., *Proc. ODP, Init. Repts.*, 139: College Station, TX (Ocean Drilling Program), 55–97.
- , 1997. Explanatory notes. In Eberli, G.P., Swart, P.K., Malone, M.J., et al., *Proc. ODP, Init. Repts.*, 166: College Station, TX (Ocean Drilling Program), 43–65.
- , 2001. Explanatory notes. In Christie, D.M., Pedersen, R.B., Miller, D.J., et al., *Proc. ODP, Init. Repts.*, 187, 1–42 [CD-ROM]. Available from: Ocean Drilling Program, Texas A&M University, College Station TX 77845-9547, USA.
- Shipley, T.H., Ogawa, Y., Blum, P., et al., 1995. *Proc. ODP, Init. Repts.*, 156: College Station, TX (Ocean Drilling Program).
- Wyllie, M.R.J., Gregory, A.R., and Gardner, L.W., 1956. Elastic wave velocities in heterogeneous and porous media. *Geophysics*, 21:41–70.

Figure F1. Configuration of the drill string used for Leg 196 logging operations. ADN = azimuthal density neutron tool, ISONIC = IDEAL sonic-while-drilling velocity tool, MWD = measurement-while-drilling tool, RAB = resistivity-at-the-bit tool.

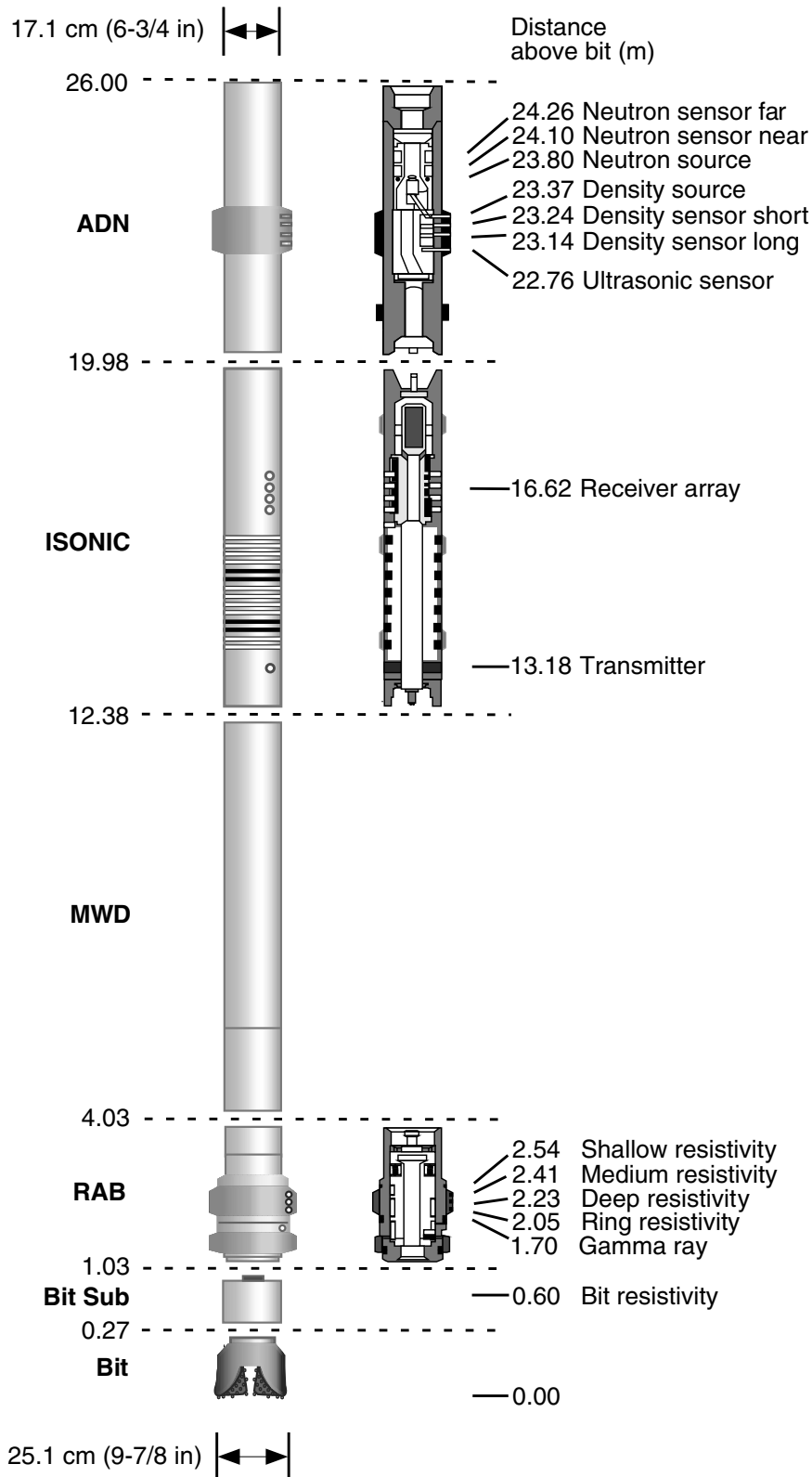


Figure F2. Schematic figure of rig instrumentation, illustrating sensor locations for surface and downhole weight-on-bit (DWOB), downhole torque (DTOR), heave, and acceleration that were used in these experiments.

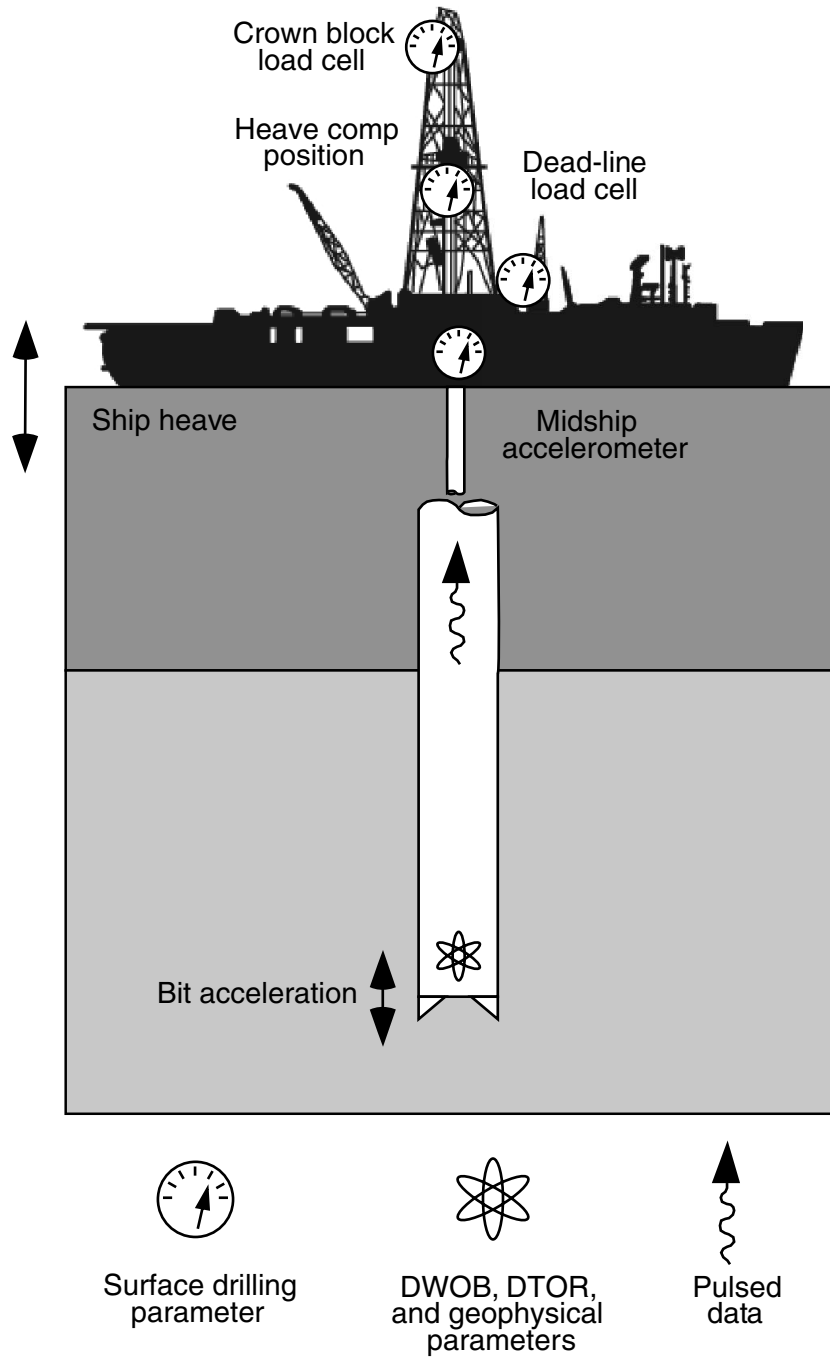


Figure F3. Position and components of the resistivity-at-the-bit (RAB) tool.

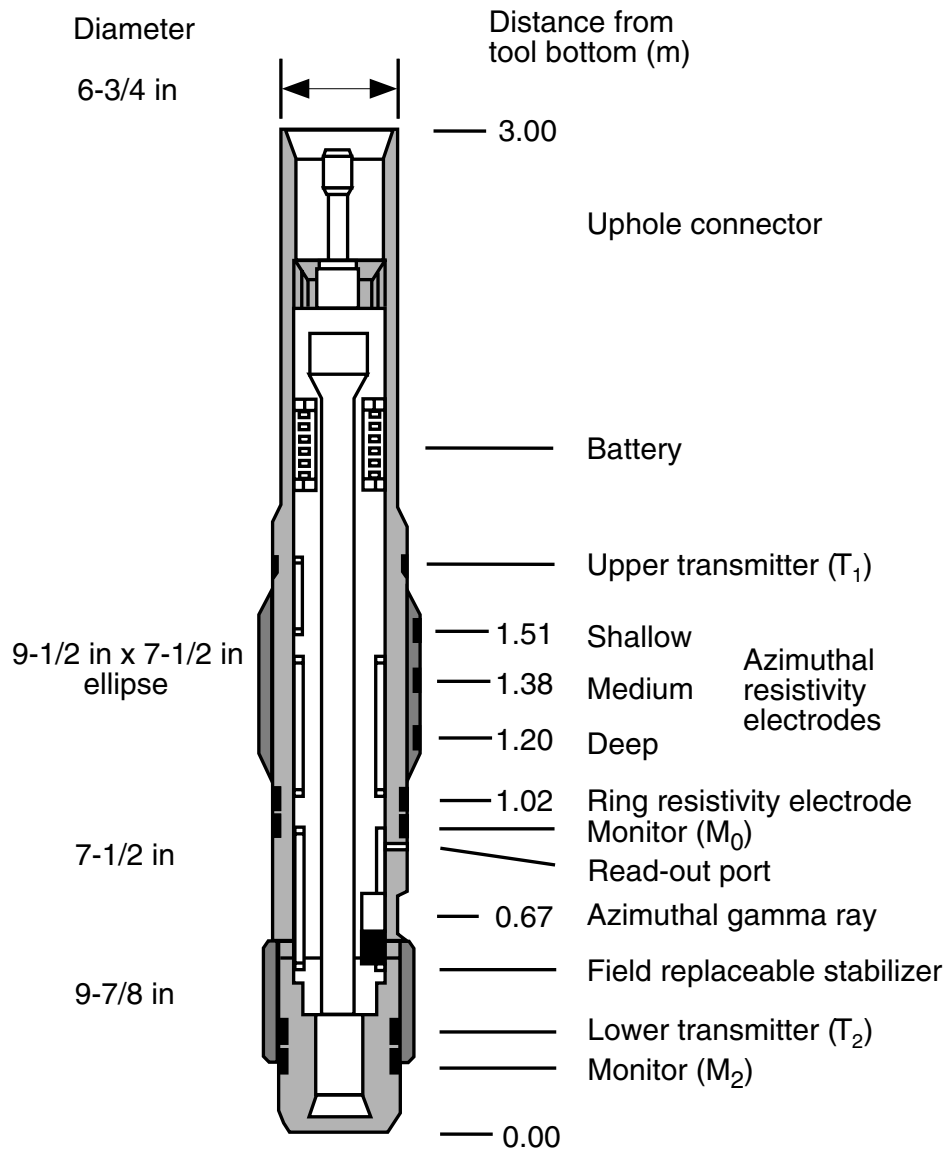


Figure F4. Configuration and principle of the measurement-while-drilling (MWD) tool.

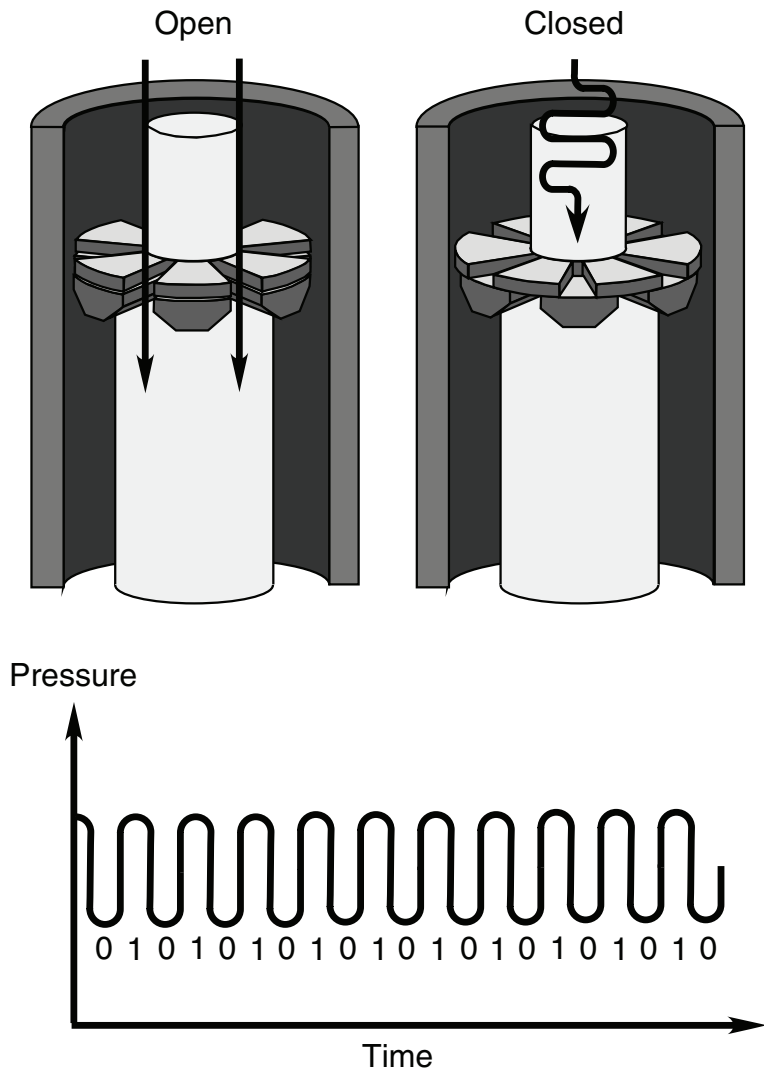


Figure F5. Position and components of the IDEAL sonic-while-drilling (ISONIC) velocity tool.

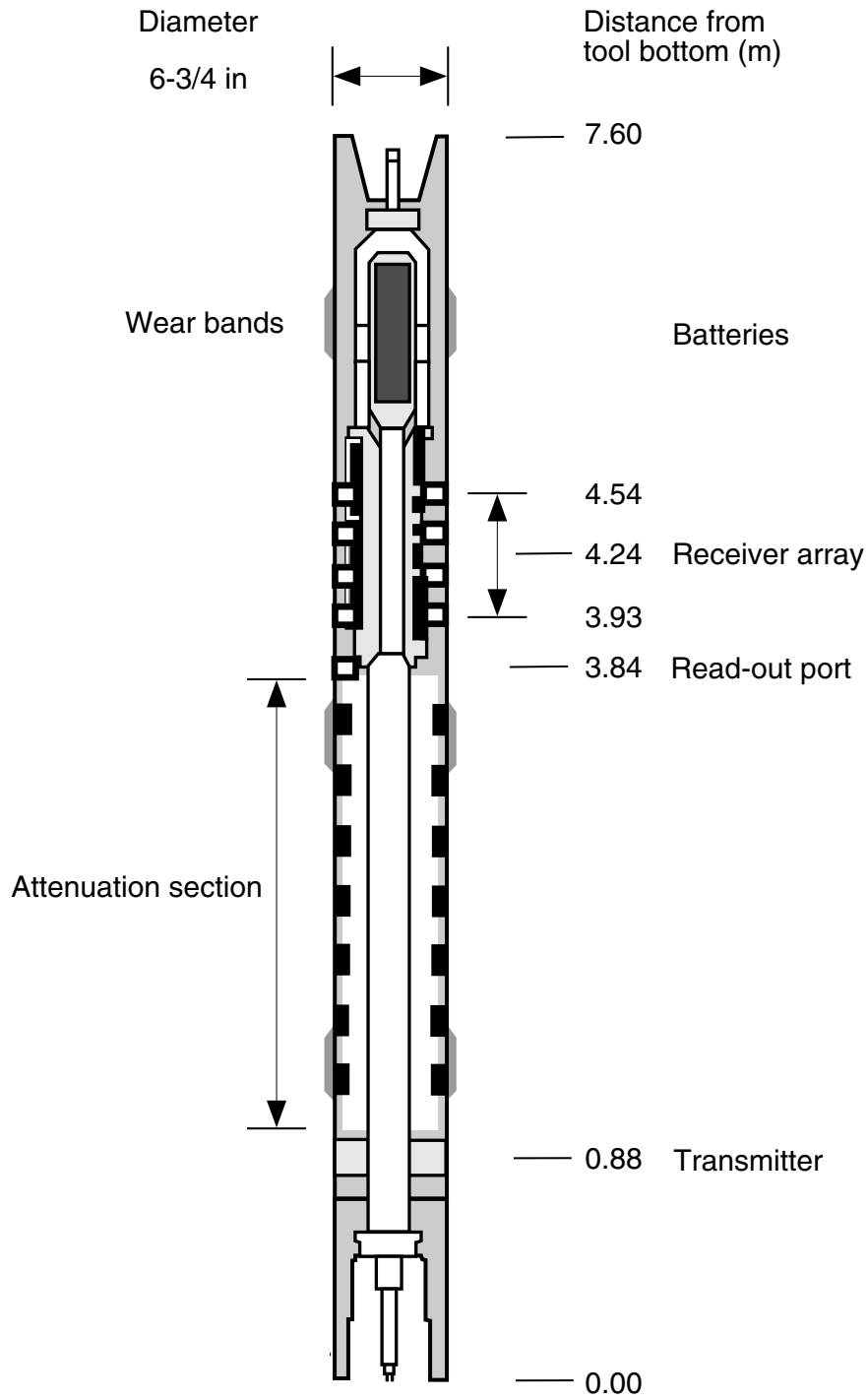


Figure F6. Position and components of the azimuthal density neutron (ADN) tool.

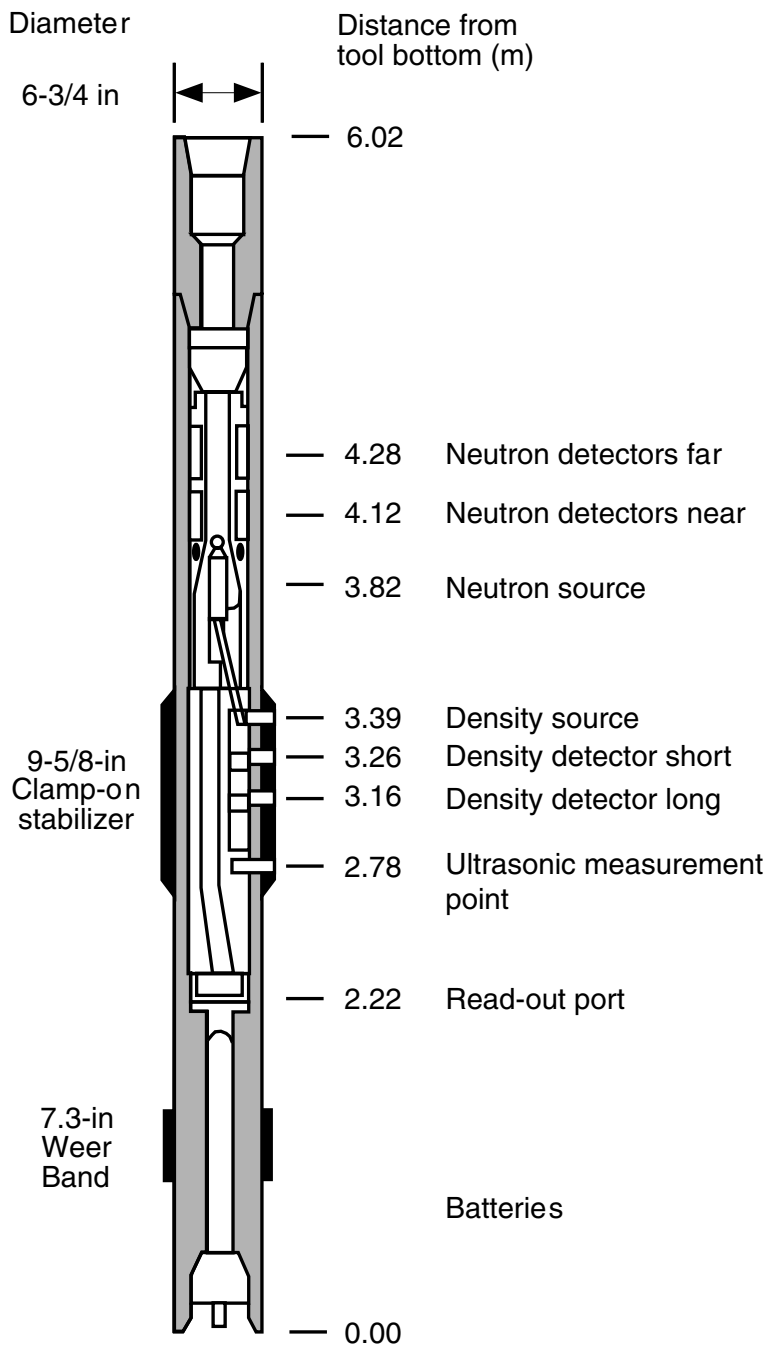


Figure F7. Onboard data flow during Leg 196. LWD = logging-while-drilling data, MWD = measurement-while-drilling data, PC = personal computer, IDEAL = Anadrill Integrated Drilling Evaluation and Logging system, DHML = Downhole Measurements Laboratory, RAB = resistivity at the bit, 2-D = two dimensional, 3-D = three dimensional.

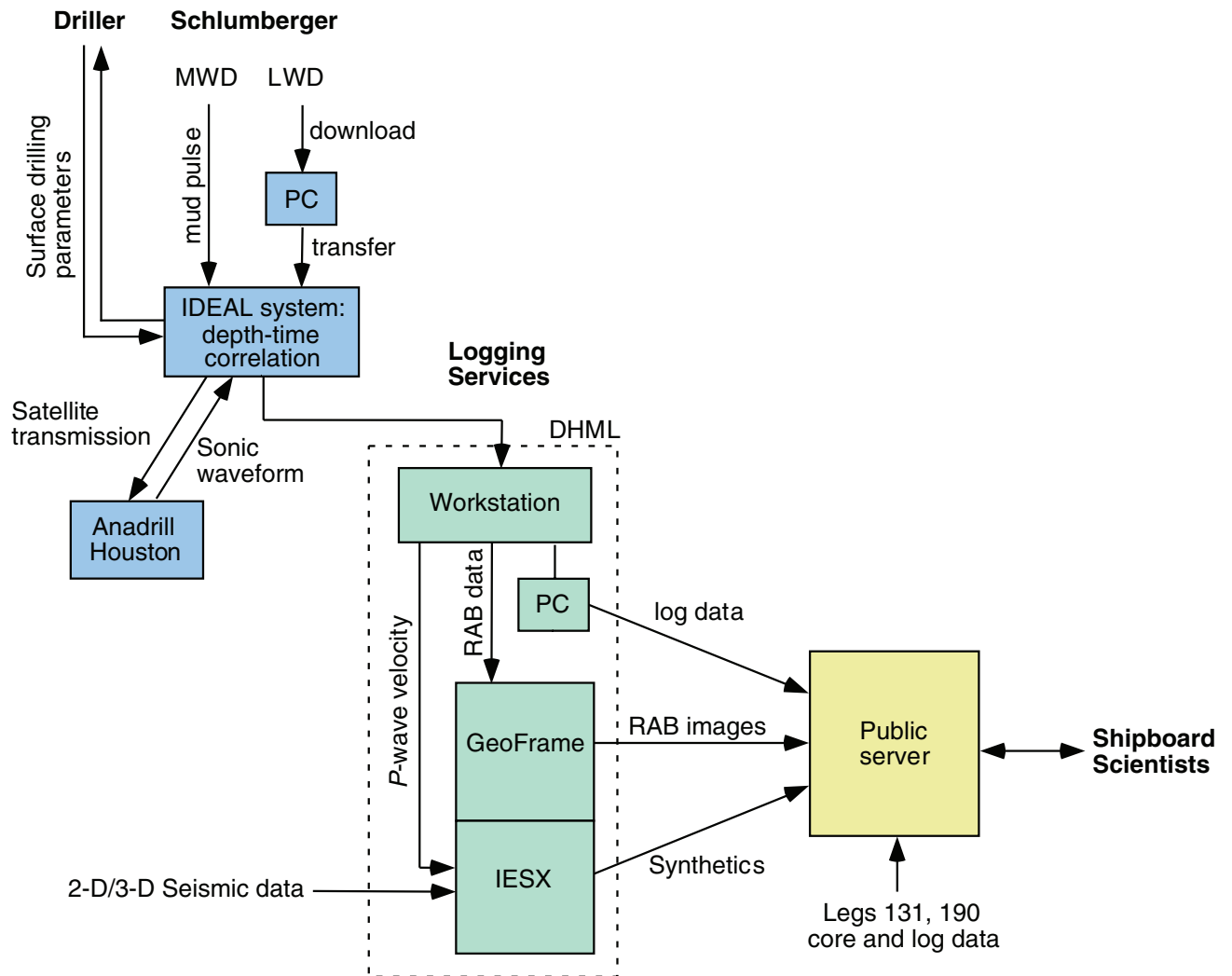
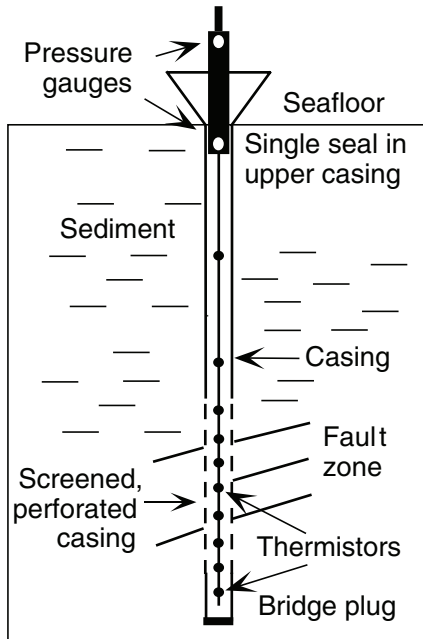


Figure F8. Schematic of original CORK hydrogeologic observatory as typically configured for an accretionary prism setting.

Schematic of CORK hydrogeological observatory



Motivation: seal reentry holes to prevent hydrologic "contamination" and allow reestablishment of in situ conditions, with:

- Long-term monitoring of temperature/pressure for:
 - Background in situ values
 - Hydrologic transients
 - Subsurface tidal loading effects
 - Responses to earthquakes
- Sampling of formation fluids
- Hydrologic testing of formation

14 CORKs deployed during 1991–2001, in subduction settings (left) and sedimented young oceanic crust

Figure F9. Consecutive stages in the installation of the Advanced CORKs (ACORKs) at Nankai Trough during Leg 196. A. Installing reentry cone and 20-in casing. (Continued on next six pages.)

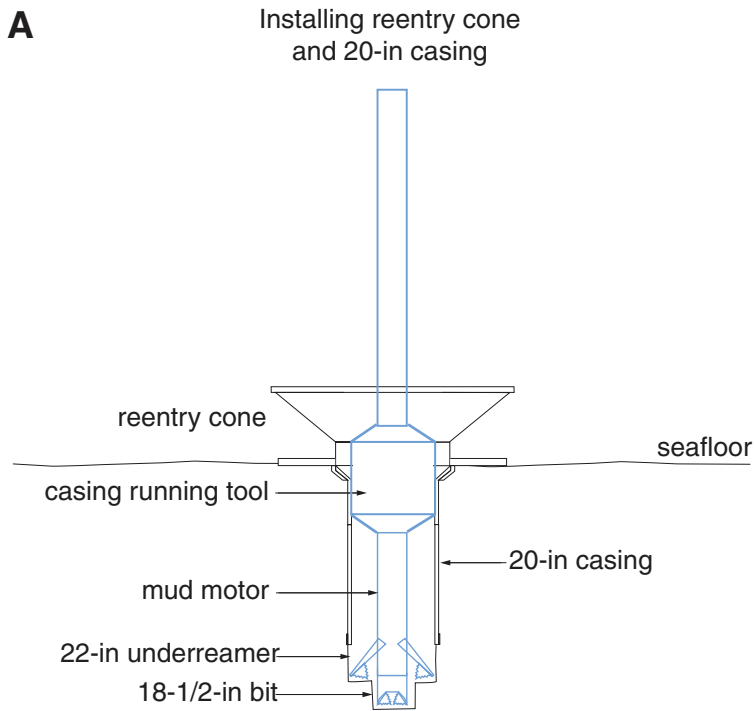


Figure F9 (continued). B. Logging-while-drilling (LWD) operations.

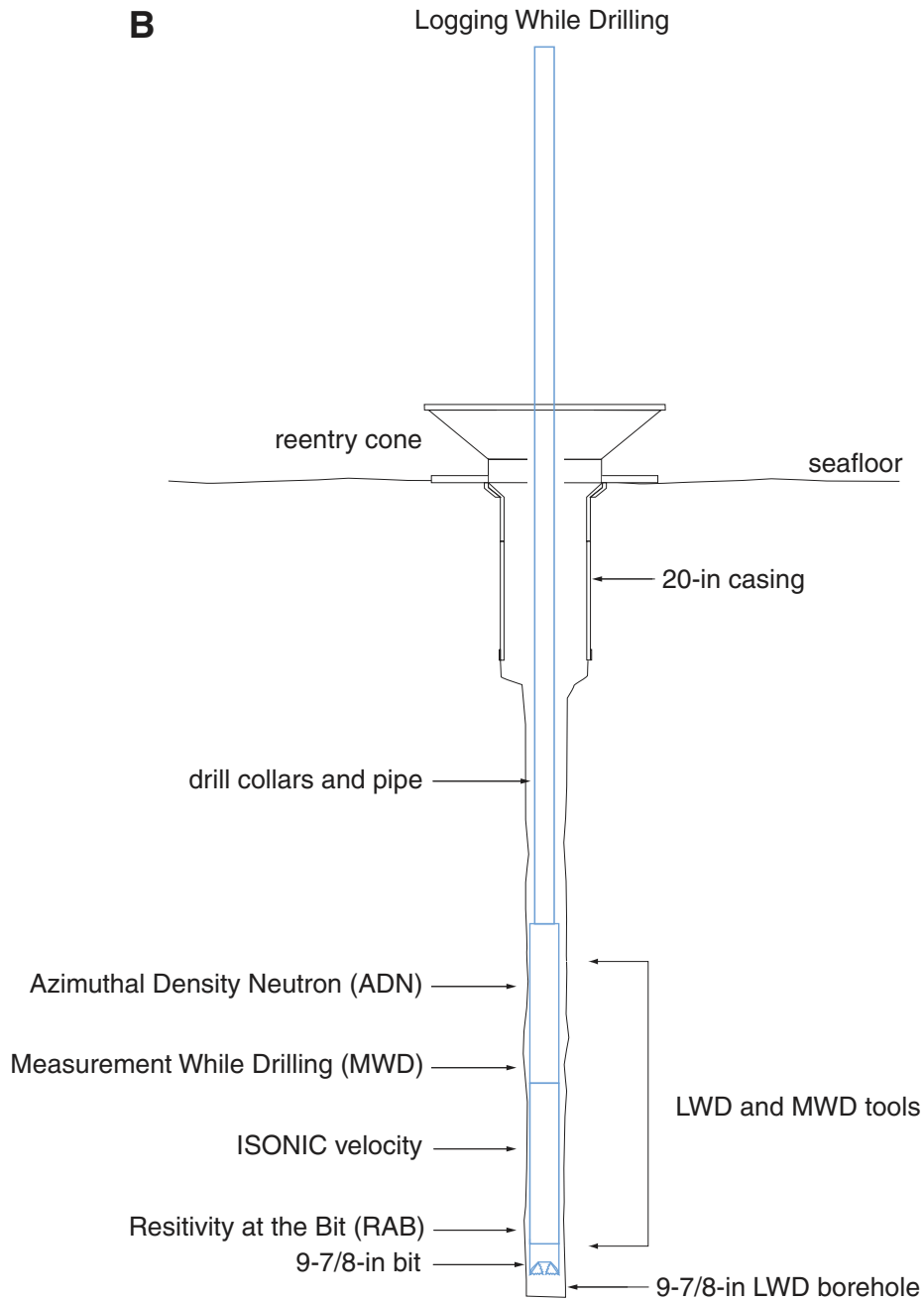


Figure F9 (continued). C. Opening LWD hole with pilot bit and 17½-in hole opener.

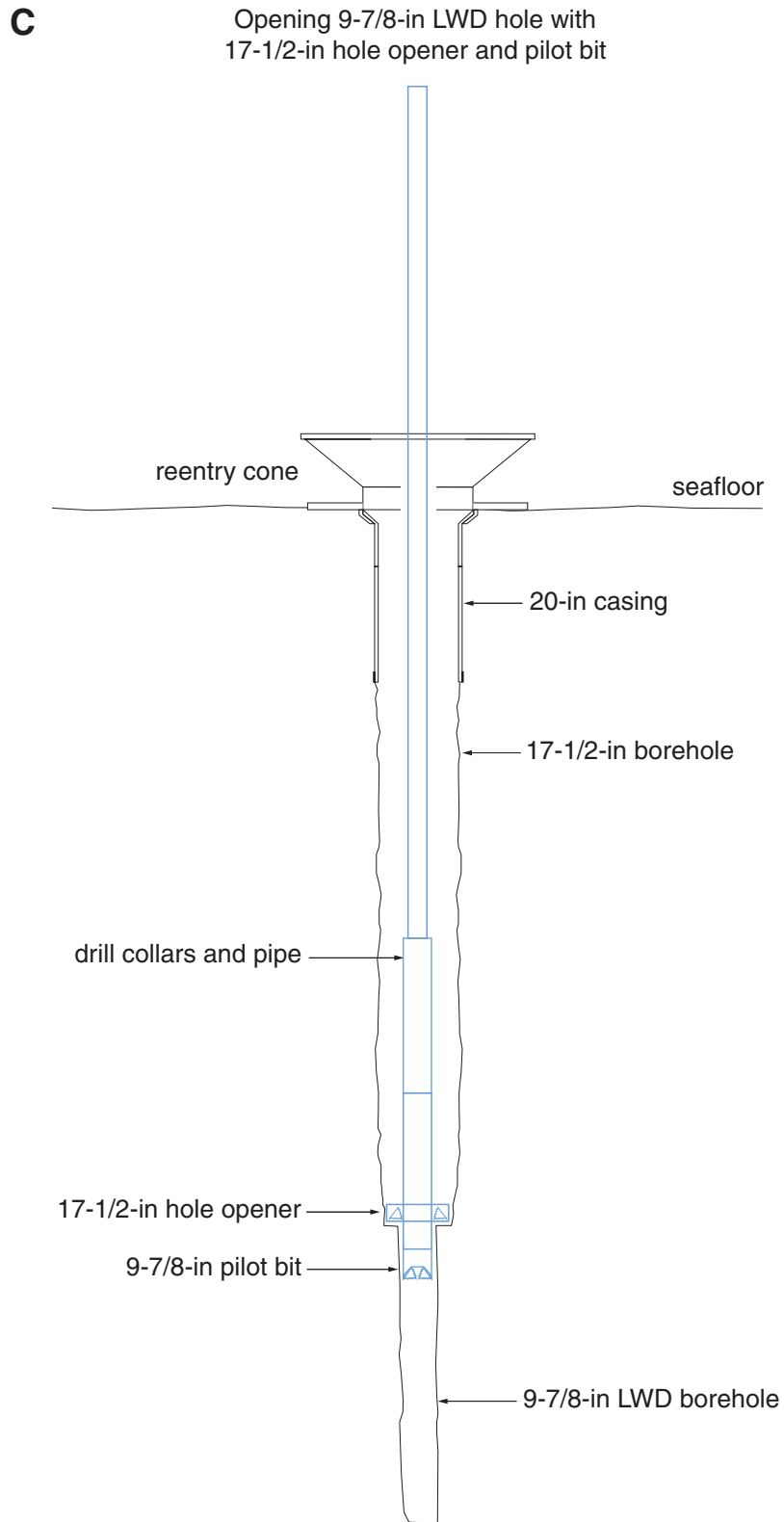


Figure F9 (continued). D. ACORK drill-in assembly with underreamer.

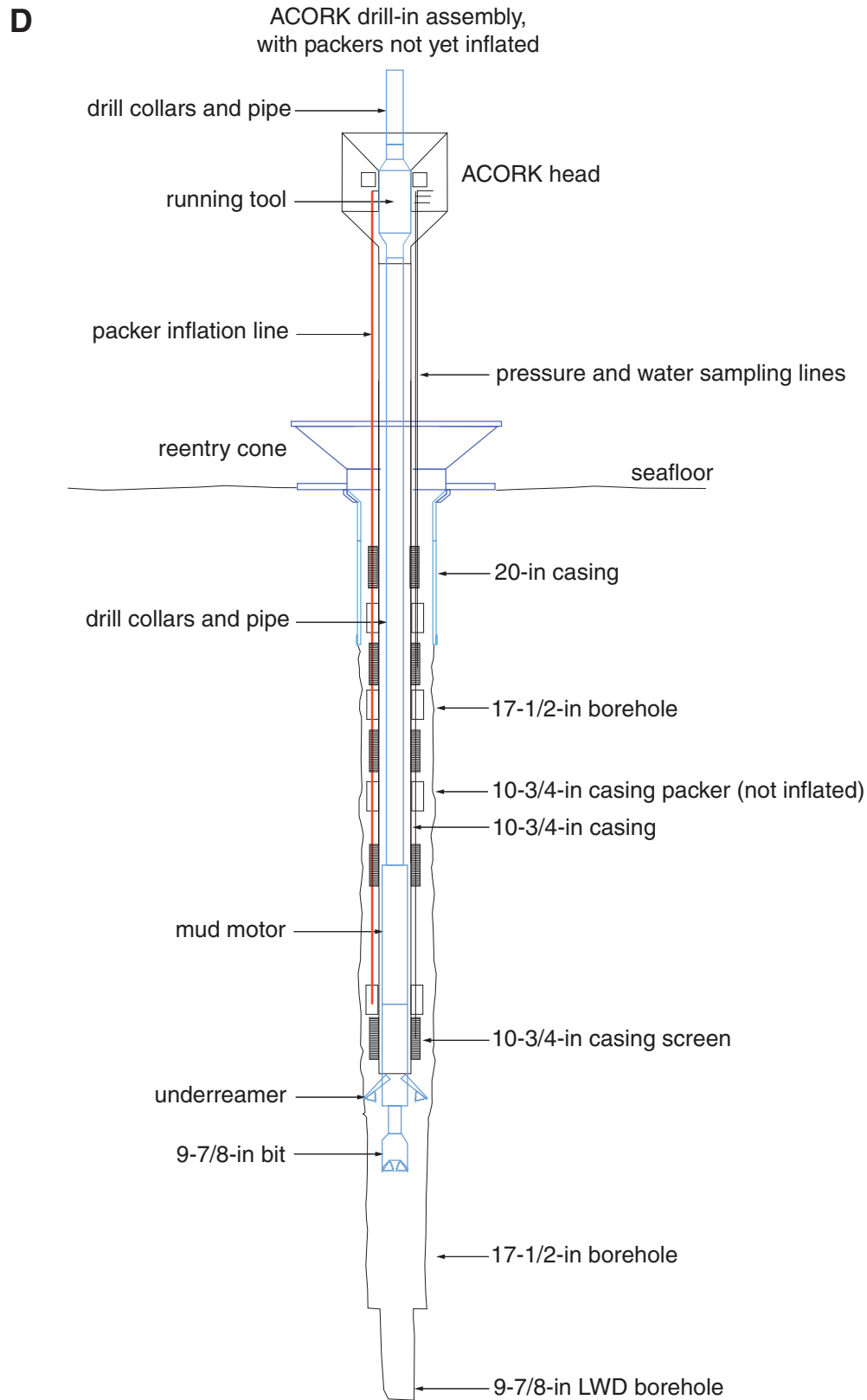


Figure F9 (continued). E. Packers inflated after ACORK drilled into place.

E

ACORK emplaced drill-in assembly,
with packers inflated

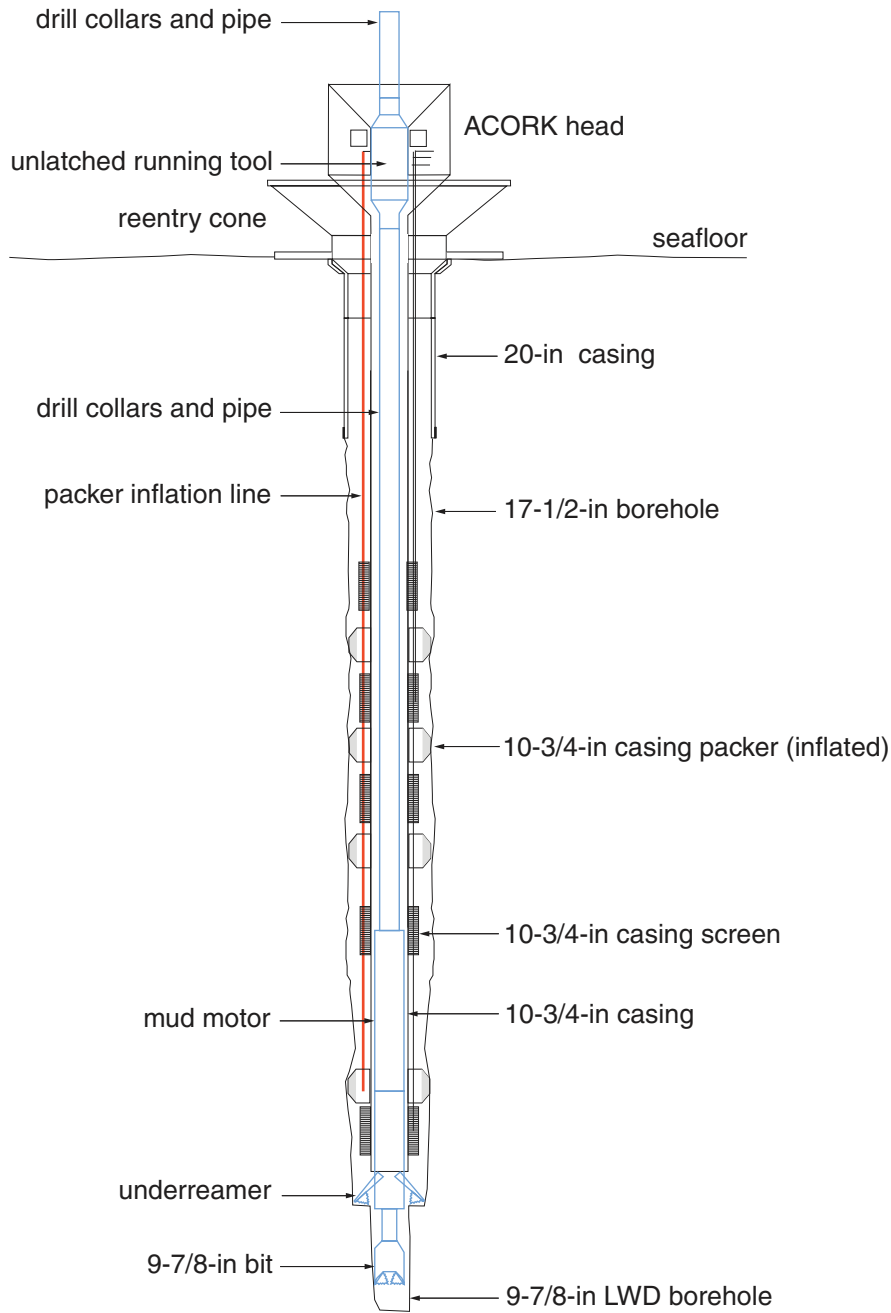


Figure F9 (continued). F. ACORK running tool released with drill-in assembly partially withdrawn.

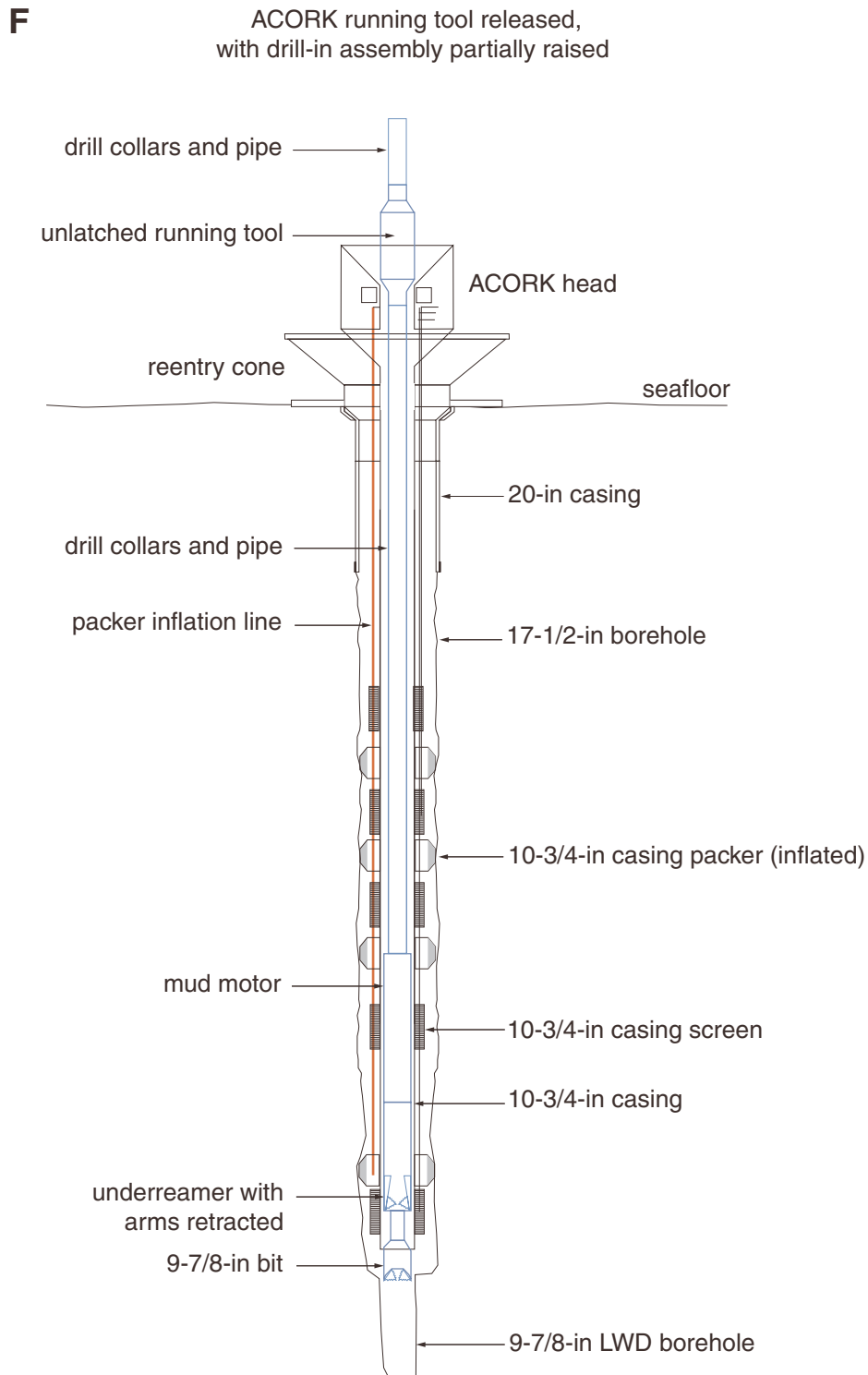


Figure F9 (continued). G. ACORK fully installed.

G

ACORK assembly installed

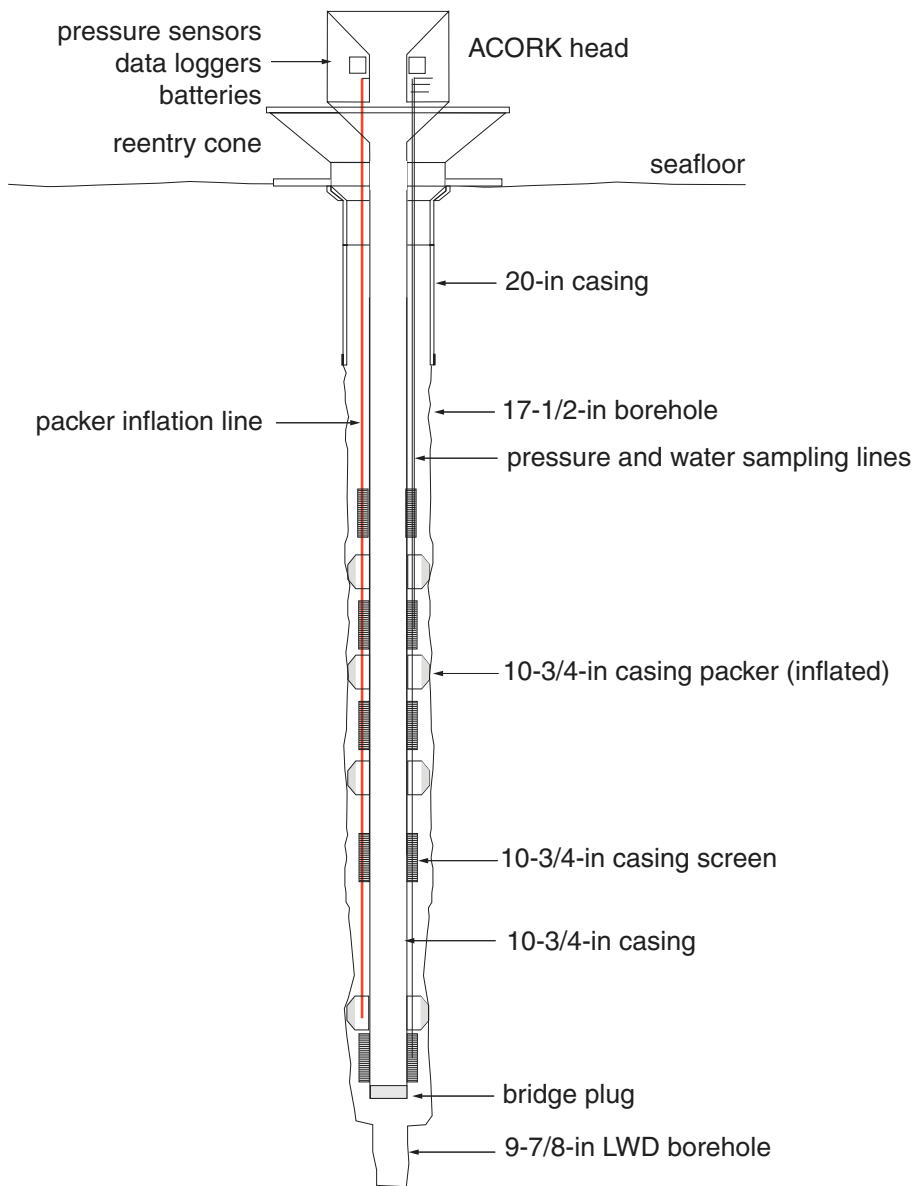


Figure F10. Photograph of ACORK head showing the three instrument bays as identified in Figure F11, p. 46. A. Bay #3 on left and #1 on right. B. Bay #2.

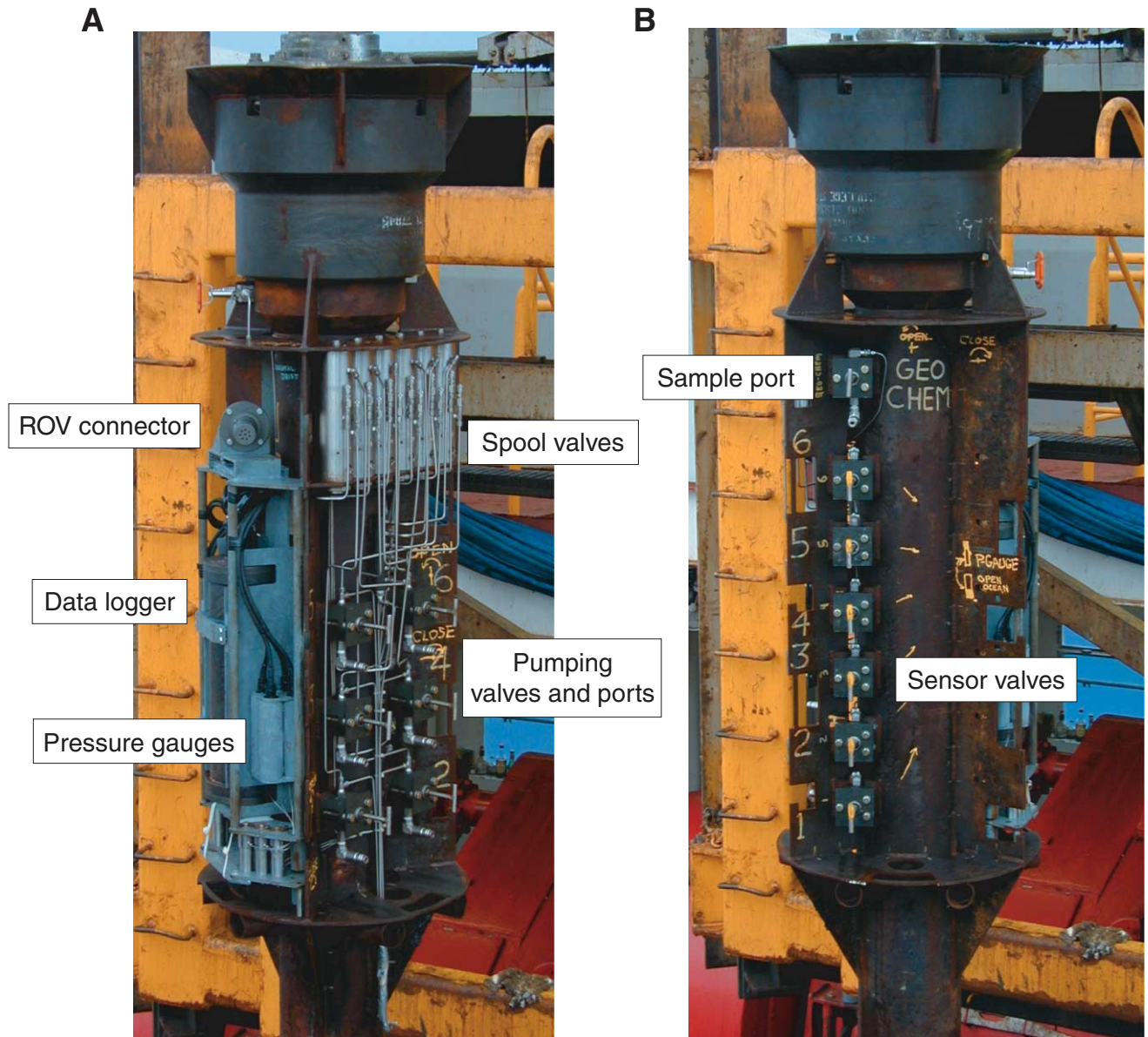


Figure F11. ACORK plumbing schematic. During installation, circulation from the drill ship is routed to the mud motor at the bottom of the casing string. Use of a “go-devil” allows this circulation to be diverted (dashed line) to fill the packers, then to shift the spool valves from their initial deployment position (dashed line) to their monitoring position (solid line).

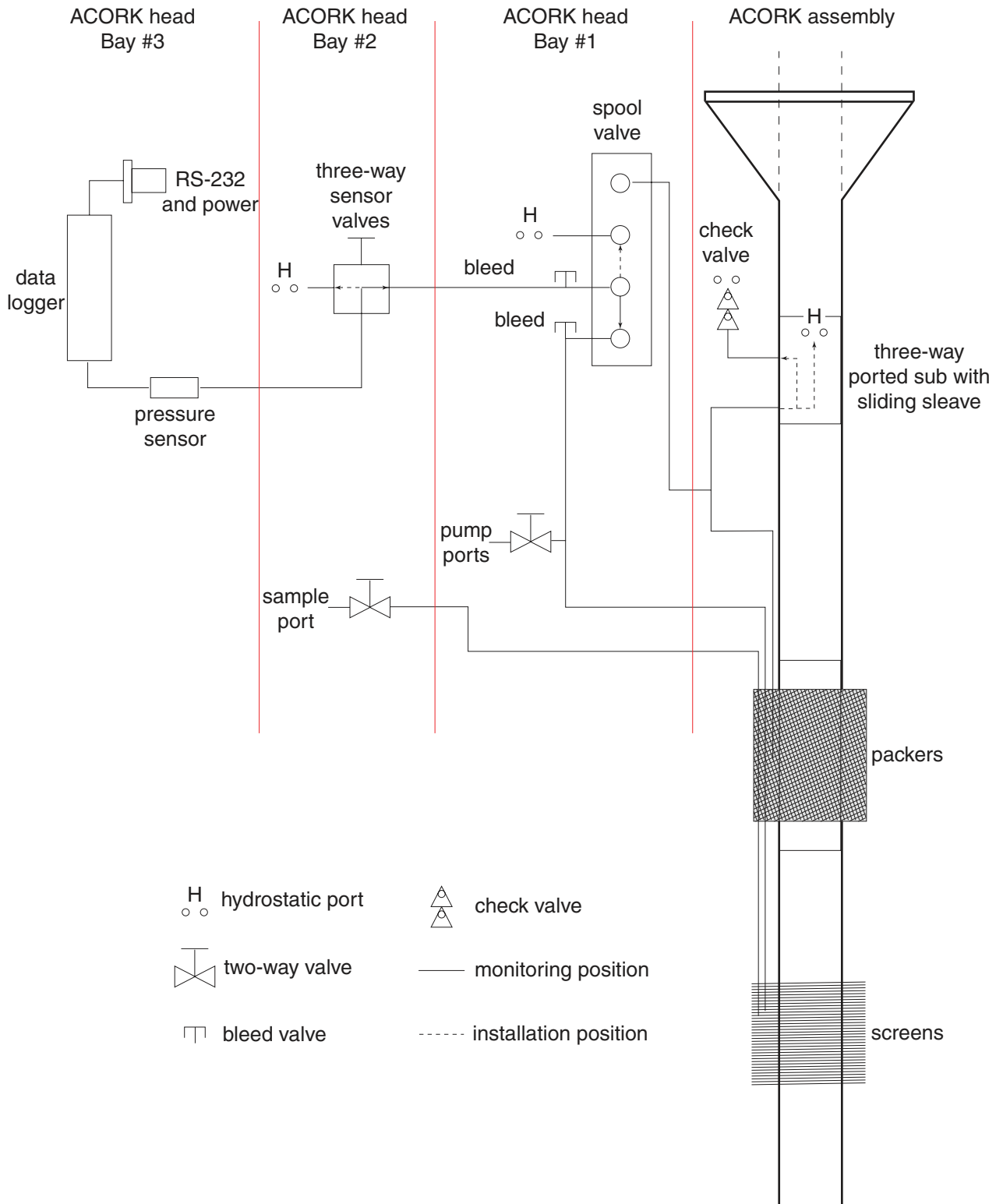


Figure F12. Igneous texture and structure definitions and abbreviations.

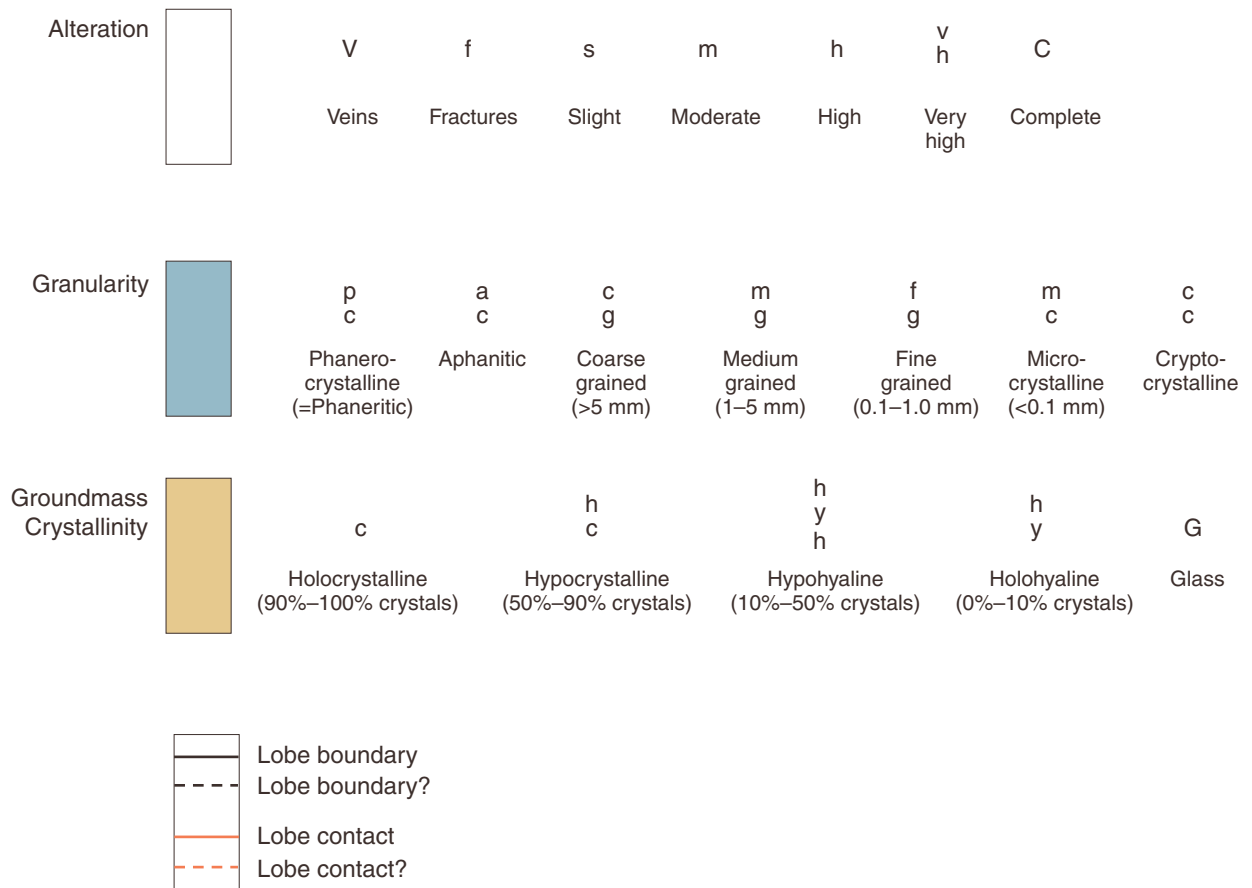


Table T1. Acronyms and units used for logging-while-drilling tools.

Tool	Output	Explanation	Unit
ADN		Azimuthal density-neutron tool	
	ROMT	Density (rotationally processed)	g/cm ³
	RHOB	Density (average bulk density)	g/cm ³
	TNPH	Thermal neutron porosity	pu
	PEF	Photoelectric effect	b/e ⁻
ISONIC		IDEAL sonic-while-drilling tool	
	DTRA	Delta-time receiver array	m/s
	ITT	integrated transit time	s
RAB		Resistivity-at-the-bit tool	
	GR	Total gamma ray	API
	RING	Ring resistivity	Ωm
	BIT	Bit resistivity	Ωm
	R _{BS}	Shallow-focused button resistivity	Ωm
	R _{MS}	Medium-focused button resistivity	Ωm
	R _{DS}	Deep-focused button resistivity	Ωm
	RAB images		
Quality control logs			
	ROP*5	5-ft averaged rate of penetration	m/hr
	RPMRAB	Rotational speed	rpm
	GTAB	Gamma ray time after bit	min
	RTAB	Ring time after bit	min
	CHRA	ISONIC coherence receiver array	
	ISTAB	ISONIC time after bit	min
	DRHO	Bulk density correction	g/cm ³
	DCAL	Differential caliper	in
	DTAB	Density time after bit	min
	NTAB	Neutron after bit	min

Note: IDEAL = Anadrill Integrated Drilling and Logging system.

Table T2. Vertical resolution and depth of investigation of resistivity-at-the-bit (RAB) measurements.

RAB measurement		Vertical Resolution (in)	Depth of investigation (in)
Button	Shallow focused	2-3	1
	Medium focused	2-3	3
	Deep focused	2-3	5
Ring		2-3	7
Bit		12-24	12

Table T3. Acronyms and units used for measurement-while-drilling (MWD) tools.

MWD tool	Drilling parameter	Unit	Sampling interval (s)	Spacing (m)
DWOB	Downhole weight on bit	klbf	4.86	0.03
DTOR	Downhole torque	kft-lbf	41.33	0.29
MWDGEN3	Bit bounce	klbf	41.33	0.29
MWDGEN1	Tool stick slip		82.67	0.57

Table T4. Measured and known thermal conductivities of half-space standards.

Standard	Conductivity (W/[m·K])		Standard deviation	Number of measurements
	Known	Measured		
Red rubber	0.96*	0.886	0.021	12
Macor	1.65†	1.65	0.004	4

Notes: Probe used = H19608. * = ODP Leg 139 (Shipboard Scientific Party, 1992), † = Blum (1997).

Table T5. Inductively coupled plasma–atomic emission spectrometry parameters*.

Element	Instrument detection limit (ppb)	Wavelength (nm)	Slit width (nm) [†]	Integration time per calculation point (s)	Voltage (V)	Mode	Increment between points (nm) [‡]	Calculation (pts)
Al	2.8	396.152	20/16	0.5	731	2	0.0270	5
Ca	0.2	393.366	20/16	0.5	351	2	0.0180	5
Fe	6.2	259.940	20/16	4.0	732	5	0.0020	1
K	60	766.490	20/16 Alk	0.5	993	2	0.0022	5
Mg	1.6	285.213	20/16	4.0	553	5	0.0022	1
Mn	1.4	257.610	20/16	4.0	643	5	0.0020	1
Na	69	589.592	20/16 Alk	0.5	632	2	0.0021	5
P	272	178.229	20/16	0.5	933	2	0.0018	5
Si	12	251.611	20/16	0.5	612	2	0.0028	5
Si	16	212.412	20/16	0.5	652	2	0.0030	5
Si	27	288.158	20/16	0.5	623	2	0.0029	5
Ti	3.8	334.941	20/16	0.5	651	2	0.0018	5
Ba	1.3	455.403	20/16	4.0	622	5	0.0250	1
Co	6	213.856	20/16	0.5	625	2	0.0021	5
Cr	7	267.716	20/16	4.0	993	5	0.0190	1
Cu	5.4	324.754	20/16	0.5	625	2	0.0019	5
Nb	36	309.418	20/16	0.5	625	2	0.0030	5
Nb	71	322.548	20/16	0.5	625	2	0.0028	5
Ni	15	231.604	20/16	0.5	990	2	0.0021	1
Sc	1.5	361.384	20/16	4.0	753	5	0.0018	1
Sr	0.4	407.771	20/16	0.5	572	2	0.0026	5
V	7.5	292.402	20/16	4.0	993	5	0.0021	1
Y	3.5	371.030	20/16	4.0	693	5	0.0027	1
Zn	1.8	213.856	20/16	0.5	625	2	0.0030	5
Zr	71	343.823	20/16	0.5	673	2	0.0018	5

Notes: * = BAS192 method acquisition parameters of analyses conducted during Leg 197. † = the widths of the entrance and exit slits. ‡ = the increment between points is the interval in nanometers between each of the calculation points in Mode 2, or the calculation window (nanometers) that constitutes the single point in Mode 5. Alk = an increase in sheath gas flow from 0.15–0.2 to 0.8 L/min for analysis of these elements.

Table T6. Typical inductively coupled plasma-atomic emission spectrometry values of reference standards*.

	BHVO-2A	BHVO-2B	Average	Certified value	BIR-1A	BIR-1B	Average	Certified value	JB-1AA	JB-1AB	Average	Certified value
Major oxides (wt%):												
SiO ₂	49.15	49.39	49.27	49.85	47.11	47.18	47.14	47.95	52.24	52.08	52.16	52.16
TiO ₂	2.79	2.77	2.78	2.69	0.96	0.96	0.96	0.96	1.3	1.3	1.3	1.3
Al ₂ O ₃	13.37	13.03	13.20	13.85	15.7	15.5	15.6	15.5	14.51	14.51	14.51	14.51
Fe ₂ O ₃	12.35	12.55	12.45	12.23	12.2	11.9	12.1	11.3	8.7	9.5	9.1	9.1
MnO	0.16	0.17	0.16	0.17	0.18	0.18	0.18	0.175	0.14	0.16	0.15	0.15
MgO	7.07	6.97	7.02	7.31	9.7	9.4	9.5	9.7	7.87	7.63	7.75	7.75
CaO	11.18	10.99	11.09	11.33	13.2	13.0	13.1	13.3	9.29	9.17	9.23	9.23
Na ₂ O	2.16	0.73	1.44	2.29	1.82	1.72	1.77	1.82	2.74	2.63	2.68	2.74
K ₂ O	0.55	-0.01	0.27	0.54	BDL	BDL	BDL	0.03	1.46	1.45	1.46	1.46
P ₂ O ₅	0.28	0.28	0.28	0.27	BDL	BDL	BDL	0.021	0.26	0.26	0.26	0.26
Total:	99.06	96.87	97.96	100.53	100.86	99.84	100.35	100.756	98.53	98.67	98.60	98.66
Trace elements (ppm):												
Ni	121	120	120	121	189	184	187	166	143	137	140	140
Cr	266	254	260	289	407	393	400	382	401	429	415	415
V	317	343	330	317	375	365	370	313	198	242	220	220
Zr	180	192	186	179	12	13	13	15.5	144	148	146	146
Sc	31.9	33.0	32.4	31.8	48	47	47	44	29	29	29	29
Y	30.1	28.9	29.5	27.6	13	16	15	16	28	20	24	24
Sr	382	389	385	403	107	107	107	108	441	445	443	443
Ba	133	135	134	139	5	6	6	7	565	429	497	497
Nb	36	39	38	19	39.5	36.0	37.8	0.6	25	29	27	27
Co	56	55	55	45	50	52	51	52	38.2	40.8	39.5	39.5
Cu	225	224	225	136	176	181	179	126	70.1	40.9	55.5	55.5
Zn	108	110	109	105	79	67	73	71	76	88	82	82

Notes: * = Leg 197 standards. Values in italics indicate that the instrument software crashed during the analysis of these elements. Iron is represented as Fe³⁺. JB-1a was used as the calibration standard. BDL = below detection limit.